

The Aerodynamics of Snowflakes and Fractal Structures:
Stokes-Flow Simulation Study

University of Warwick

Lewis Arnold

March 2023

Abstract

Drag calculations are presented for Stokes flow around self-similar fractals of spheres in the continuum regime using the method of fundamental solutions and method of reflections. A power law relationship is also established that relates the drag on the fractal to its fractal dimension. For fractals that possess symmetries, the resistance matrix is determined to be diagonal, resulting in the drag experienced by these fractals being independent of their orientation. The meshfree approach to the fluid simulation is found to be accurate and computationally efficient, however, ill-conditioning of the MFS matrix is observed if the simulation parameters are not selected appropriately. Improvements on the standard method of reflections are implemented such as a relaxation factor and a cutoff value. The impact of these tools on the accuracy of the solutions and the conditioning of the MFS matrix are evaluated.

Contents

Abstract	i
List of Figures	v
List of Tables	vi
1 Introduction	1
2 Literature Review	3
2.1 Stokes Flow	3
2.2 Method of Fundamental Solutions	4
2.3 Fractal Aggregate Geometry	5
2.4 Unanswered Questions	8
3 Numerical Methodology	10
3.1 Aggregate Generation	10
3.1.1 Generating the Aggregates	10
3.1.2 Calculating Fractal Dimension	11
3.2 Fluid Simulation	12
3.2.1 Method of Fundamental Solutions (MFS)	13
3.2.2 Method of Reflections (MOR)	15
3.2.3 Validation, Verification and Parameter Selection	17
4 Results and Analysis	23
4.1 Integer Dimension Aggregates	23
4.1.1 Chain	24
4.1.2 Square	26
4.2 2D Fractal Aggregates	27
4.2.1 Vicsek Fractal	27
4.2.2 Sierpinski Triangle Fractal	28

4.2.3	Sierpinski Triangle Fractal - 2	29
4.3	3D Fractal Aggregates	30
4.3.1	3D Vicsek Fractal	31
4.3.2	Sierpinski Tetrahedron Fractal	32
4.3.3	Sierpinski Tetrahedron Fractal - 2	33
5	Discussion	34
5.1	Power Law Relationship	34
5.2	Symmetry	35
5.3	Drag Ratio	36
6	Conclusions and Recommendations for Further Work	37
A	Self-Affine Fractals	i
A.1	2D Fractal-4	i
A.2	3D Fractal-4	iii
B	Additional Drag Plots	iv
B.1	Large Aggregates	iv
B.2	Drag Ratios	ix
C	Streamlines	xi

List of Figures

2.1	Stokes flow around a sphere (Zhao, 2016).	4
2.2	Scaling geometry (Falconer, 2004).	5
2.3	Vicsek fractal (Meakin, 1987).	6
2.4	Mobility ratio $\beta = \frac{R_m}{R_g}$ against number of monomers N in the continuum limit for different types of aggregate clusters (Sorensen, 2011).	8
3.1	First three iterations of the Vicsek fractal.	10
3.2	Fractal generation code.	11
3.3	Fractal dimension calculation code.	12
3.4	Point force in a fluid (Lockerby, 2022a).	13
3.5	Singularity sites and boundary nodes on a particle (Lockerby, 2022a).	14
3.6	Number of nodes against error and processing time.	18
3.7	Distribution of sites on a circular disk (Cheng and Hong, 2020).	19
3.8	Effect of relaxation factor on the convergence of MFS for a chain of 15 touching spheres.	20
3.9	Effect of relaxation factor on the convergence of MFS for a fractal (Vicsek fractal, Iteration 3).	21
4.1	Chain extending in the x-direction.	24
4.2	Drag versus number of spherules in a chain extending in the x-direction.	24
4.3	Drag versus number of spherules in a chain extending in the x-direction on loglog plots with fitted curves.	25
4.4	Drag ratio versus number of spherules in a chain.	25
4.5	Square in the x-y plane.	26
4.6	Drag versus number of spherules in a square in the x-y plane on loglog plots with fitted curves.	26
4.7	Drag ratio versus number of spherules in a square.	27
4.8	Vicsek fractal in the x-y plane.	27
4.9	Drag versus number of spherules in the Vicsek fractal in the x-y plane on loglog plots with fitted curves.	28

4.10 Sierpinski triangle in the x-y plane.	28
4.11 Drag versus number of spherules in a 2D-fractal in the x-y plane on loglog plots with fitted curves.	29
4.12 2D-fractal in the x-y plane.	29
4.13 Drag versus number of spherules in a 2D-fractal in the x-y plane on loglog plots with fitted curves.	30
4.14 3D fractal.	31
4.15 Drag versus number of spherules in a fractal on a loglog plot with a fitted curve. . . .	31
4.16 Sierpinski tetrahedron.	32
4.17 Drag versus number of spherules in a fractal on a loglog plot with a fitted curve. . . .	32
4.18 3D fractal.	33
4.19 Drag versus number of spherules in a fractal on a loglog plot with a fitted curve. . . .	33
5.1 $\frac{1}{D_f}$ against x for the large aggregate case.	34
5.2 Drag against rotation angle for the Sierpinski fractal (Iteration 3).	35
A.1 2D-fractal in the x-y plane.	i
A.2 Drag versus number of spherules in a 2D-fractal in the x-y plane on loglog plots with fitted curves.	ii
A.3 3D fractal.	iii
A.4 Drag versus number of spherules in a fractal on a loglog plot with a fitted curve. . . .	iii
B.1 Drag versus number of spherules in the Vicsek fractal.	v
B.2 Drag versus number of spherules in the Sierpinski triangle fractal.	vi
B.3 Drag versus number of spherules in the Sierpinski triangle fractal - 2.	vii
B.4 Drag versus number of spherules in the 3D Vicsek fractal.	viii
B.5 Drag versus number of spherules in the 3D Sierpinski tetrahedron fractal.	viii
B.6 Drag versus number of spherules in the 3D Sierpinski tetrahedron fractal - 2.	ix
B.7 Drag ratio versus number of spherules in 2D fractal aggregates.	x
C.1 Streamlines around a chain of spheres.	xi
C.2 Streamlines around the Vicsek fractal.	xii

List of Tables

3.1 Effect of ζ on the convergence of MFS for a fractal (Vicsek fractal, Iteration 3)	20
3.2 Effect of cutoff on error and processing time of MFS for a fractal (Vicsek fractal, Iteration 3)	22

Chapter 1

Introduction

This project aims to further understanding of the aerodynamics of fractal geometries that occur frequently in nature. Although this project focuses on the simplest case, Stokes flow in the continuum regime, developments of the methods used in this project would make many aerodynamic simulations more efficient. For example, research from Stein et al. (2015) found that snowflakes possess these fractal properties. This can be used to better predictions of snowflake motion by simplifying the shapes to a set of rules that can be easily computed. This improves on current climate model parameterisations of snowflakes that have proven difficult to determine due to irregularities in their shape that result in vastly different aerodynamics (McCorquodale and Westbrook, 2021). The method of fundamental solutions can be used to further reduce the computational power required to find the drag on the fractal aggregates.

In addition to climate models on Earth, more accurate snowflake parameterisations can be applied to a wide range of scenarios. A more abstract application of the dynamics of fractal structures is to the largest of the Solar System's moons, Ganymede – a satellite of Jupiter. It has an internal magnetic field that arises due to its fluid iron core. Iron snow forms at the outer core due to crystallisation and melts as it approaches the inner core, resulting in compositional convection (Christensen, 2015). Although this example falls into the realm of magnetohydrodynamics, a deeper understanding of how fractal aggregates can be modelled could be used to reduce the computational power required to determine flow in these conditions.

It is also understood that soot particles are fractal aggregates of spherules. Atmospheric soot is the second-largest anthropogenic contributor to global warming; however, its radiative effects have been difficult to accurately estimate due to its complex morphologies (Luo et al., 2021). Soot formation is strongly intercoupled with the aerodynamics of soot particles following combustion. Understanding the relationship between the soot's fractal dimension and drag would advance knowledge of how particles travel and develop in the atmosphere, which has implications on the aforementioned radiative effects. Despite soot typically experiencing turbulent flow, simulations of soot as fractals would be a cheaper and more accurate approach for predicting drag.

The report is organised as follows. In Chapter 2, a literature review is conducted on Stokes flow, the method of fundamental solutions and fractal aggregate geometries in order to ascertain the progress made in these fields and what unanswered questions remain. In Chapter 3, the methodology is detailed. This involves both how self-similar fractal aggregates were generated and how the fluid was simulated. In Chapter 4, the MFS is used to solve Stokes flow problems involving different aggregates. In Chapter 5, the trends found in the results were further explored. In particular, the power law relationship, effect of symmetry on drag and the drag ratio were examined.

Chapter 2

Literature Review

2.1 Stokes Flow

Stokes flow concerns the movement of a fluid when the Reynolds number is much less than 1 ($Re \ll 1$). The Reynolds number is a dimensionless quantity that characterises the ratio of inertial forces to viscous forces within the fluid.

$$Re = \frac{\rho UL}{\mu} \quad (2.1)$$

The numerator is composed of the density ρ , velocity U and characteristic length L . The denominator is the dynamic viscosity of the fluid μ . Typically, the motion of an incompressible, Newtonian fluid is described by the following Navier-Stokes equations.

$$\nabla \cdot \mathbf{u} = 0 \quad (2.2)$$

$$\rho \frac{D\mathbf{u}}{Dt} = \mathbf{F} - \nabla p + \mu \nabla^2 \mathbf{u} \quad (2.3)$$

Eq. 2.2 is the continuity equation and Eq. 2.3 is the conservation of momentum equation where \mathbf{F} is the body force per unit volume (Guazzelli and Morris, 2011). The Stokes approximation - a scaling argument - states that when the velocity and characteristic length are small, and the dynamic viscosity is high, the inertial forces can be neglected and the Stokes equations are obtained (Eq. 2.2 and Eq. 2.4).

$$\begin{aligned} \nabla \cdot \mathbf{u} &= 0 \\ -\nabla p + \mu \nabla^2 \mathbf{u} &= \mathbf{0} \end{aligned} \quad (2.4)$$

The Stokes approximation fails to account for weak inertial effects that affect the flow field at distances far from the particle, however, near the particle of interest the Stokes equations hold

(Guazzelli and Morris, 2011).

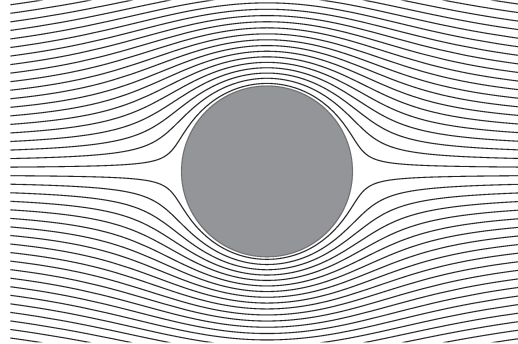


Figure 2.1: Stokes flow around a sphere (Zhao, 2016).

The total hydrodynamic force \mathbf{F} experienced by a suspended particle (Figure 2.1) is the surface integral of the dynamic stress σ acting normal \mathbf{n} to the surface Ω of the particle.

$$\mathbf{F} = \int_S \sigma \cdot \mathbf{n} d\Omega \quad (2.5)$$

The dynamic stress tensor is defined as $\sigma = \sigma^a + \rho \mathbf{g} \cdot \mathbf{x} \mathbf{I}$ where σ^a is the absolute stress tensor which contains the sum of the deviatoric (viscous) stresses and the pressure acting on an infinitesimal element of fluid.

$$\sigma^a = \begin{bmatrix} -p + \tau_{xx} & \tau_{yx} & \tau_{zx} \\ \tau_{xy} & -p + \tau_{yy} & \tau_{zy} \\ \tau_{xz} & \tau_{yz} & -p + \tau_{zz} \end{bmatrix} \quad (2.6)$$

The second term $\rho \mathbf{g} \cdot \mathbf{x} \mathbf{I}$ contains the forces acting on the element due to gravity - these forces (per unit volume) are often ignored for simplicity.

An important result that was established by Sir George Gabriel Stokes in 1851 is the drag on a spherical particle in Stokes flow - namely Stokes Law (Stokes et al., 1851).

$$\mathbf{F} = -6\pi\mu\mathbf{u}d \quad (2.7)$$

The drag on a sphere in Stokes flow is proportional to the dynamic viscosity of the fluid μ , the relative velocity of the sphere \mathbf{u} , and the characteristic length of the sphere d .

2.2 Method of Fundamental Solutions

In order to solve the Stokes equations (Eq. 2.2 and Eq. 2.4) for drag, the method of fundamental solutions (MFS) was utilised in the project. The MFS is a type of boundary method that can be

used to numerically solve linear partial differential equations (Fairweather and Karageorghis, 1998). As such, the MFS can be applied to Stokes flow due to the property of linearity of the equations that arises from neglecting inertial forces in the fluid. This method is similar to the Boundary Element Method (BEM) since both methods use fundamental solutions, which by definition, always satisfy the governing equations.

To determine the unique solution for different geometries, boundary conditions are satisfied using a superposition of fundamental solutions (Stokeslets). The primary advantage of the MFS is in the formation of the boundary conditions at ‘boundary nodes’ or ‘collocation points’. Unlike typical CFD methods such as the finite volume method that discretizes 3D space, the MFS is a ‘meshfree’ method that discretizes the surface of the geometry. This significantly improves computational efficiency since the method reduces the spatial dimensions from 3 to 2 (Cheng and Hong, 2020).

The boundary conditions are solved using a number of ‘singularity sites’ or ‘source points’ located on a pseudo-boundary. An additional advantage of the method is the ability of choosing the location of these sites. However, if the site positions are not chosen carefully the equations may become non-invertible. Furthermore, it suffers with an uncertainty principle that has been observed in a variety of meshfree methods. That is, by increasing the accuracy of the solutions, convergence becomes slow due to ill-conditioning of the MFS matrix (Alves, 2009).

2.3 Fractal Aggregate Geometry

Aggregation occurs frequently in nature whereby solid particles come together to form aggregates. A significant amount of literature has been published demonstrating that these particles, despite appearing complex, can be characterised by a fractal (Hausdorff) dimension (Jungblut et al., 2019). This characteristic is scale invariant as it expresses how efficiently the constituent particles are packed together. The Hausdorff dimension extends the notion of Euclidean (integer) dimensions that are well understood.

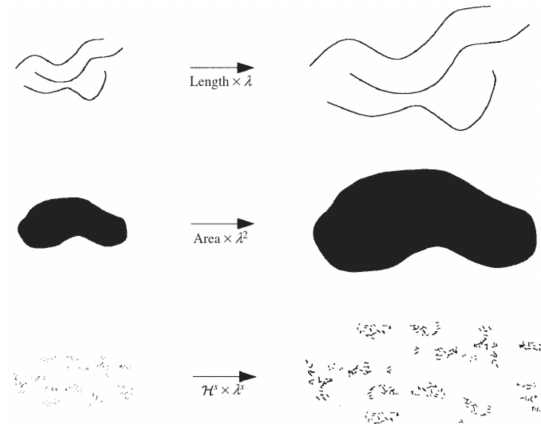


Figure 2.2: Scaling geometry (Falconer, 2004).

When scaled by a factor S , the length of a line increases by a factor S , the area of a 2D plane increases by a factor S^2 and the volume of a 3D object increases by a factor S^3 (Falconer, 2004). Similarly, the mass of a D_f -dimensional object increases by a factor S^{D_f} . For self-similar fractals, a power law emerges that relates the number of constituent units N_{unit} , the scaling factor S and the fractal dimension D_f . The scaling factor relates the length scale of the fractal on the current iteration to the constituent units. Each unit is equivalent to the previous iteration of the fractal.

$$N_{unit} = S^{D_f} \quad (2.8)$$

The advantage of restricting the geometries in the project to self-similar fractals, where fractals are formed using a scaled-down version of itself, is the reduction in computational time required for simulation (Xu and Fan, 2014).

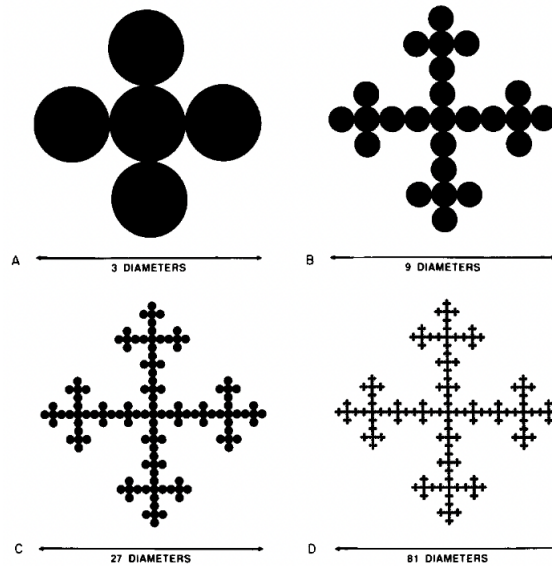


Figure 2.3: Vicsek fractal (Meakin, 1987).

The following equation is a more useful rearrangement of the relationship between the aforementioned properties, which allows the fractal dimension to be easily calculated for a self-similar fractal.

$$D_f = \frac{\log(N_{unit})}{\log(S)} \quad (2.9)$$

Consider the Vicsek fractal in Fig. 2.3, where the unit initially consists of 5 particles. To form the next iteration of the aggregate, 5 of these units are placed in the same arrangement as the particles in the original unit. A consequence of this is that each consecutive iteration, the size of the aggregate increases by a factor of 3. Using Eq. 2.9, the fractal dimension is $D_f = \log(\frac{25}{5})/\log(\frac{18}{6}) = \log(5)/\log(3) \approx 1.46$ (Meakin, 1987).

Previous simulations of fractal aggregates use spherical primary particles, commonly named spherules, to approximate the particles composing the aggregate. These particles are assumed to have point contacts and have the same size a . The radius of gyration R_g is typically used to quantify the size of the aggregate. Unlike Eq. 2.8 which describes the power relationship for only self-similar fractals, a similar power law can be derived for general fractal aggregates (Sorensen, 2011).

$$N = k_0 \left(\frac{R_g}{a} \right)^{D_f} \quad (2.10)$$

Here, N is the number of monomers and k_0 is the scaling prefactor for the relationship. Although this prefactor has not been fully interpreted, some evidence suggests that it relates to the packing fraction of the aggregate. This is a function of the fractal dimension and the type of packing that constitutes the aggregate. Since the simulation of aggregates involves the use of a finite number of monomers, calculations of k_0 and D_f have not yielded asymptotic, which has limited the success in gaining a greater understanding of how the fractal dimension and prefactor influence the structure of the ensemble (Heinson et al., 2012). It is evident that an aggregate is only truly fractal in the limit $N \rightarrow \infty$, however, the assumption is typically made that an aggregate consisting of $N > 3$ can be considered fractal-like (Sorensen, 2011). Using the radius of gyration to determine the fractal dimension, does not result in a constant fractal dimension for each iteration. However, as the number of iterations is increased, the fractal dimension approaches a limit.

Due to the deterministic, self-similarity of the particles considered in this project, the size of the aggregate can be defined by the maximum distance between points on the aggregate instead of the radius of gyration. This is advantageous as determining the fractal dimension using the the maximum distance is constant for each iteration.

Another important concept used to evaluate mobility properties such as drag, lift and pitching moments is the mobility radius R_m of an aggregate. The mobility radius is the radius of a sphere R that yields the same drag coefficient C_D as the aggregate of interest.

$$C_D(R) = C_D(R_m) \quad (2.11)$$

Research by Sorensen found that the relationship between the number of primary particles and the mobility radius are as follows,

$$N \propto R_m^{D_m} \quad (2.12)$$

$$R_m \propto N^x \quad (2.13)$$

D_m is the mass-mobility scaling exponent and $x = 1/D_m$ is the mobility-mass scaling exponent. In the continuum regime where the Knudsen number $Kn \ll 1$, the mobility radius is proportional to the radius of gyration by the mobility ratio (or the hydrodynamic ratio) β (Sorensen, 2011).

$$R_m = \beta R_g \quad (2.14)$$

Eq. 2.14 arises from dimensional arguments whereby the medium is assumed to have no length scale and the fractal aggregate is sufficiently large that the length scale of the primary particles can be neglected. If the mobility ratio β is constant then $D_m = D_f$. An important quantity to note is the limiting case of a mobility ratio for a single sphere which is $\beta = \sqrt{\frac{5}{3}} \approx 1.29$ since $R_g = \frac{3}{5}R$ (Sorensen, 2011).

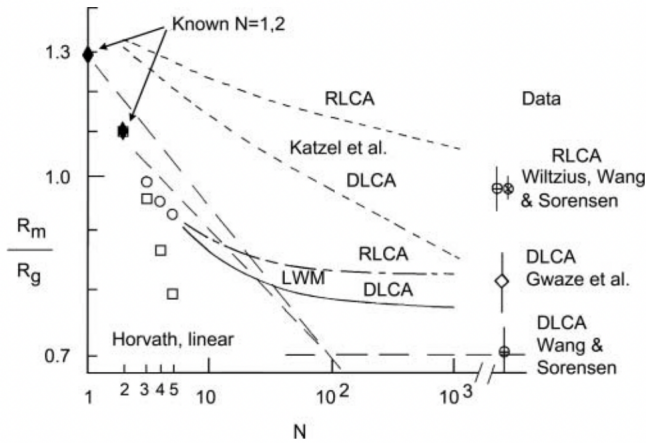


Figure 2.4: Mobility ratio $\beta = \frac{R_m}{R_g}$ against number of monomers N in the continuum limit for different types of aggregate clusters (Sorensen, 2011).

Although both the radius of gyration are important concepts in the analysis of fractal aggregates, due to the assumption of self-similarity, they are not the focus of this research project.

2.4 Unanswered Questions

Despite a significant amount of research on drag experienced by fractal aggregates, the effect of fractal dimension on drag remains poorly understood. This can be rewritten to find the expected relationship between drag and the number of primary particles. Stokes Law can be applied to a fractal through the mobility radius of the hydrodynamically equivalent sphere.

$$\mathbf{F}_{drag} = 6\pi\mu\mathbf{u}R_m \quad (2.15)$$

Due to Stokes Law, drag is proportional to the mobility radius of the aggregate, so it follows from Eq. 2.13 that,

$$\mathbf{F}_{drag} \propto N^x \quad (2.16)$$

As the fractal aggregate becomes sufficiently large, there is only one length scale in the problem which results in a constant mobility ratio. If there is a constant mobility ratio ($D_f = D_m$), then Eq. 2.16 can be rewritten as,

$$\mathbf{F}_{drag} \propto N^{\frac{1}{D_f}} \quad (2.17)$$

Through calculating the drag acting on simulations of self-similar fractal aggregates, the aim is to confirm Eq. 2.17. The hypothesis was that the drag on larger fractal aggregates (where $n > 100$ and the mobility ratio becomes constant) is proportional to the number of monomers raised to the reciprocal of the fractal dimension (Figure 2.4).

Chapter 3

Numerical Methodology

The method for the project can be split up into two overarching sections - the generation of the aggregates and the simulation of Stokes flow.

3.1 Aggregate Generation

All aggregates that were generated were agglomerates of touching spheres - monomers, primary particles or spherules. The advantage of using spheres as the primary particles is the ability to normalise the drag results for the aggregates by using the drag on a single sphere which has an analytical solution. Also, only one matrix inversion is required for the method of reflections (MOR) when using particles with the same geometry (Lockerby, 2022b).

3.1.1 Generating the Aggregates

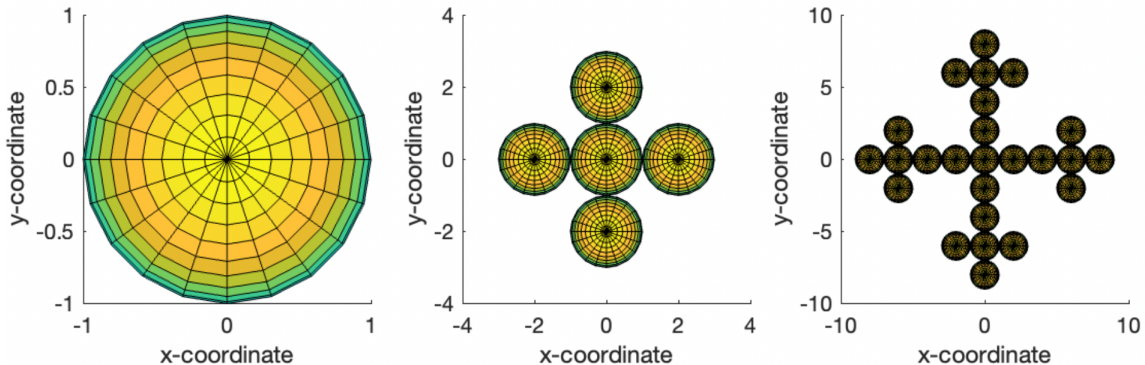


Figure 3.1: First three iterations of the Vicsek fractal.

The aggregates were formed using an iterative method starting with just a single sphere with a radius of 1 unit for the first iteration. The second iteration stored the pattern that formed the

basis for all further iterations to generate fractal structures. This was created by defining the centre positions of all the spheres in the aggregate. The minimum spacing between spheres was 2 sphere radii since this separation resulted in the spheres touching. For each subsequent iteration, the aggregate generated on the previous iteration formed the new base unit for the new iteration. The code used to generate the Vicsek fractal, displayed in Fig. 3.1, is outlined in Fig. 3.2 below.

```

1 if iteration==1
2     rSphere=[0 0 0];
3 else
4     iteration = iteration-1;
5     rSphere = zeros(5^N,3);
6     rSphere(1:5,1:3) = [0 0 0; 2 0 0; 0 2 0; -2 0 0; 0 -2 0];
7     for k = 2:iteration
8         dUnit = 2*3^(k-1);
9         rSphere(5^(k-1)+1:5^k,1:3) =
10        [[rSphere(1:5^(k-1),1)+dUnit,rSphere(1:5^(k-1),2),rSphere(1:5^(k-1),3)];
11        [rSphere(1:5^(k-1),1)-dUnit,rSphere(1:5^(k-1),2),rSphere(1:5^(k-1),3)];
12        [rSphere(1:5^(k-1),1),rSphere(1:5^(k-1),2)+dUnit,rSphere(1:5^(k-1),3)];
13        [rSphere(1:5^(k-1),1),rSphere(1:5^(k-1),2)-dUnit,rSphere(1:5^(k-1),3)]];
14    end
15 end

```

Figure 3.2: Fractal generation code.

3.1.2 Calculating Fractal Dimension

In order to investigate the relationship between the fractal dimension and the drag experienced by self-similar fractals, the fractal dimension must first be calculated. For the deterministic, self-similar fractal aggregates used in this project, the maximum distance between points on the aggregate R_{max} was used as the length scale. Despite most literature using the radius of gyration R_g as the aggregate's length scale, this is not necessary for aggregates that do not have a random nature to their generation (see Section 2.3). The fractal dimension is calculated using the factor that the number of monomers N increases by each iteration $N_{Unit} = \frac{N_i}{N_{i-1}}$ and the scale factor is a ratio of sizes of the aggregate on each iteration $S = \frac{s_i}{s_{i-1}}$.

$$D_f = \frac{\log(N_i/N_{i-1})}{\log(s_i/s_{i-1})} \quad (3.1)$$

This calculation is equivalent to Eq. 2.8. As an example, consider the second and third iteration of the Vicsek fractal, which are depicted in Fig. 3.1. As mentioned in Section 2.3, the fractal in iteration 3 consists of 5 times the number of particles in iteration 2 and the size of the aggregate has increased by a scale factor of 3. The fractal dimension is $D_f = \log(\frac{25}{5})/\log(\frac{18}{6}) = \log(5)/\log(3) \approx$

1.46 (Meakin, 1987). The code used to calculate the fractal dimension of any aggregate is outlined in Fig. 3.3 below.

```

1 n = zeros(2,1);
2 s = zeros(2,1);
3
4 for i = 1:2
5     rSphere = FractalGenerator(i+1);
6     n(i) = size(rSphere,1);
7     rMax = 0;
8     for j = 1:n(i)
9         for k = 1:n(i)
10            if j ~= k
11                rRel = norm(rSphere(k,:)-rSphere(j,:))+2;
12                if rRel>rMax
13                    rMax=rRel;
14                end
15            end
16        end
17    end
18    s(i) = rMax;
19 end
20
21 Df = \log{(n(2)/n(1))}/\log{(s(2)/s(1))}
22 Gamma = 1/Df

```

Figure 3.3: Fractal dimension calculation code.

3.2 Fluid Simulation

The calculation of drag on the aggregates relied on determining the drag on an individual spherule. The chosen method for calculating drag on a spherule was the method of fundamental solutions (MFS). The primary reason for using the MFS over the more commonly used CFD software is the reduction in computational power and cost required for simulations. In CFD, the fluid around the object is discretized into smaller regions but in the MFS approach, the surface of the object itself is discretized. This reduces the dimensionality of the the problem from 3D to 2D. Both algorithms for MFS and MOR are applications of work completed by Professor Duncan Lockerby (Lockerby, 2022a,b). In this section, up until 3.2.3, I have overviewed these methodologies.

3.2.1 Method of Fundamental Solutions (MFS)

The MFS can be uniquely applied to Stokes flow problems due to the linearity of the Stokes equations (2.2, 2.4).

$$\nabla \cdot \mathbf{u} = 0 \quad (2.2)$$

$$-\nabla p + \mu \nabla^2 \mathbf{u} = \mathbf{f} \delta(\mathbf{r}) \quad (2.4)$$

Consider the Stokes equations for a point force applied in a fluid that satisfies $Re \ll 1$ (see Fig. 3.4). The point where the force is applied is known as the ‘singularity site’ or ‘site’. It is represented by $\mathbf{f}\delta(\mathbf{r})$ where \mathbf{f} is the force vector, δ is the Dirac delta function and \mathbf{r} is the position vector. The Stokes equations to describe the flow response to a point force are,

$$\nabla \cdot \mathbf{u} = 0 \quad (2.2)$$

$$\nabla p - \mu \nabla^2 \mathbf{u} = \mathbf{f} \delta(\mathbf{r}) \quad (3.2)$$

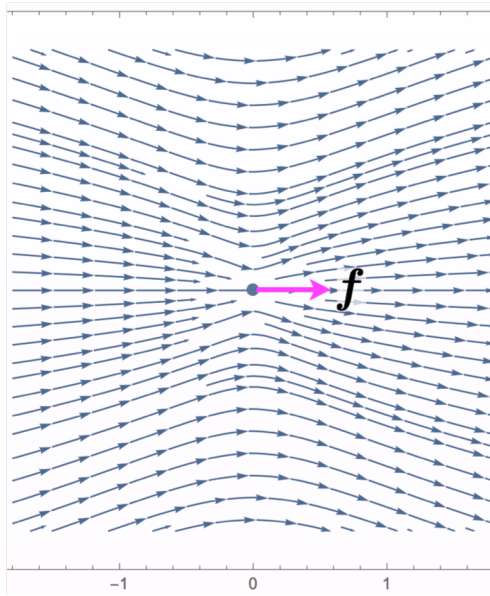


Figure 3.4: Point force in a fluid (Lockerby, 2022a).

Eq. 3.3 is a fundamental solution (primary Green’s function) of the Stokes equations - known as the Stokeslet. This gives the velocity field around a point force in Stokes flow, where \mathbb{I} is the identity matrix.

$$\mathbf{u}(\mathbf{r}) = \frac{\mathbf{f}}{8\pi\mu} \cdot \left[\frac{\mathbb{I}}{\|\mathbf{r}\|} + \frac{\mathbf{r}\mathbf{r}}{\|\mathbf{r}\|^3} \right] \quad (3.3)$$

To determine the hydrodynamic force (or drag) on a particle, a superposition of Stokelets is used to satisfy the boundary conditions at \mathcal{N} points on the surface of the particle known as ‘boundary nodes’ or ‘nodes’. The singularity sites are equally distributed inside the particle at \mathcal{M} locations on the surface of a scaled-down sphere; see Fig. 3.5. The Stokes equations become,

$$\nabla \cdot \mathbf{u} = 0 \quad (2.2)$$

$$\nabla p - \mu \nabla^2 \mathbf{u} = \sum_{i=1}^{\mathcal{M}} \mathbf{f} \delta(\mathbf{r} - \mathbf{r}_s^i) \quad (3.4)$$

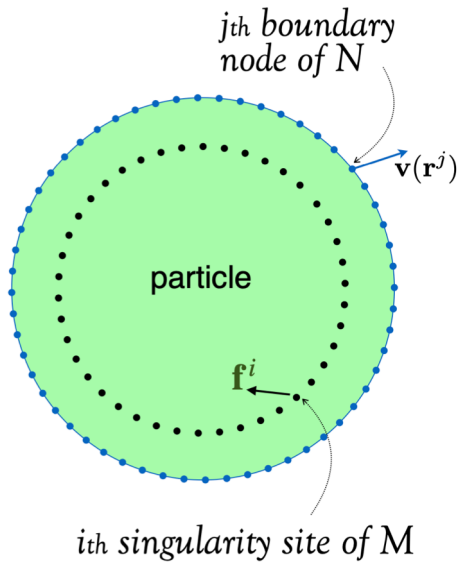


Figure 3.5: Singularity sites and boundary nodes on a particle (Lockerby, 2022a).

The total velocity field $\mathbf{u}(\mathbf{r})$ produced by the \mathcal{M} point forces (\mathbf{f}^i) located at the singularity sites (\mathbf{r}_s^i) is the superposition of the Stokeslet velocity fields:

$$\mathbf{u}(\mathbf{r}) = \frac{1}{8\pi\mu} \sum_{i=1}^{\mathcal{M}} \mathbf{f}^i \cdot \left[\frac{\mathbb{I}}{\|\mathbf{r}^i\|} + \frac{\mathbf{r}^i \mathbf{r}^i}{\|\mathbf{r}^i\|^3} \right] \quad (3.5)$$

where $\mathbf{r}^i = \mathbf{r} - \mathbf{r}_s^i$ is the position vector from the i^{th} singularity site to a point in space located at \mathbf{r} . The boundary conditions for the problem are impermeability and no-slip, which imply that there is no flow inside the particle and the velocity of the particle is equal to the velocity of the fluid at the surface of the particle. Substituting the no-slip boundary condition into Eq. 3.5 gives,

$$\mathbf{u}(\mathbf{r}^j) = \frac{1}{8\pi\mu} \sum_{i=1}^{\mathcal{M}} \mathbf{f}^i \cdot \left[\frac{\mathbb{I}}{\|\mathbf{r}^{ij}\|} + \frac{\mathbf{r}^{ij} \mathbf{r}^{ij}}{\|\mathbf{r}^{ij}\|^3} \right] \quad (3.6)$$

where $\mathbf{r}^{ij} = \mathbf{r}_b^j - \mathbf{r}_s^i$ is the position vector from the i^{th} singularity site to the j^{th} boundary node. This equation can be inverted to find the point forces at every site \mathbf{f}^i given a velocity field for the fluid. The total hydrodynamic force \mathbf{F} on the particle is then,

$$\mathbf{F} = - \sum_{i=1}^{\mathcal{M}} \mathbf{f}^i \quad (3.7)$$

To compute this inversion, Eq. 3.6 can be rewritten in the form,

$$\mathbf{u}(\mathbf{r}^j) = \sum_{i=1}^{\mathcal{M}} \mathbf{f}^i \cdot \mathbb{J}(\mathbf{r}^{ij}) \quad (3.8)$$

where

$$\mathbb{J}(\mathbf{r}^{ij}) = \frac{1}{8\pi\mu} \left[\frac{\mathbb{I}}{\|\mathbf{r}^{ij}\|} + \frac{\mathbf{r}^{ij}\mathbf{r}^{ij}}{\|\mathbf{r}^{ij}\|^3} \right]$$

By reshaping $\mathbf{u}(\mathbf{r}^j)$, \mathbf{f}^i and $\mathbb{J}(\mathbf{r}^{ij})$, Eq. 3.8 can be written in the standard matrix equation form.

$$\mathbb{A}\mathbf{x} = \mathbf{d} \quad (3.9)$$

where

$$\mathbb{A} = \begin{bmatrix} \mathbb{J}_{1,1} & \cdots & \mathbb{J}_{1,\mathcal{M}} \\ \vdots & \ddots & \vdots \\ \mathbb{J}_{\mathcal{N},1} & \cdots & \mathbb{J}_{\mathcal{N},\mathcal{M}} \end{bmatrix}, \quad \mathbf{x} = \begin{bmatrix} f_1 \\ \vdots \\ f_{\mathcal{M}} \end{bmatrix}, \quad \mathbf{d} = \begin{bmatrix} u_1 \\ \vdots \\ u_{\mathcal{M}} \end{bmatrix}$$

When $\mathcal{M} < \mathcal{N}$ (see 3.2.3), the matrix equation can be solved for a least-squares solution using a Moore-Penrose inverse.

$$\mathbf{x} = [\mathbb{A}^{-1}] \mathbf{d} \quad (3.10)$$

The drag force is the component of this force acting in the opposite direction to the velocity.

3.2.2 Method of Reflections (MOR)

The MFS is a suitable method to find the drag on a single particle; however, to find the drag on P particles this method is too costly if used alone as the matrices become too large. Although each particle interacts hydrodynamically with every other particle in the system, the MOR considers each particle in isolation and accounts for errors using an iterative process until the drag reaches a reasonable accuracy. Instead of inverting a matrix storing information about every particle in the system, only the matrices representing each individual particle need to be inverted.

As mentioned above, Eq. 3.10 is solved for each particle in isolation, so let x^n and d^n represent

the force vectors at the singularity sites and velocity vectors at the boundary nodes for the n^{th} particle. The forces calculated on the m^{th} particle affect the velocity of the fluid at the boundary nodes of the n^{th} particle. To determine the effect of these forces, let \mathbb{A}^{mn} be the matrix formed using the m^{th} particle's sites and the n^{th} particle's nodes. The algorithm is as follows (Lockerby, 2022b),

1. For $n = 1, 2 \dots P$, let $x^n = 0$ and $\tilde{d}^n = d^n$.
2. Solve the matrix equation (Eq. 3.10) for each particle in isolation.

$$\tilde{x}^n = [\mathbb{A}^{nn}]^{-1} \tilde{d}^n$$

3. Use this result to update the solution.

$$x^n \leftarrow x^n + \tilde{x}^n$$

4. Since the boundary conditions have been fully satisfied there is no residual.

$$\tilde{d}^n = 0$$

5. The velocity vector at the nodes of the m^{th} particle caused by the forces at the sites on the n^{th} particle is $\mathbb{A}^{mn}\tilde{x}^n$. The resultant velocity vector on particles $m = 1, 2 \dots P$ ($m \neq n$) is given by,

$$\tilde{d}^m \leftarrow \tilde{d}^n - \mathbb{A}^{mn}\tilde{x}^n$$

6. Repeat steps 2 to 5 until completed for all P particles.
7. Calculate the root mean square (RMS) of both \tilde{d} and d . The ratio of the two number is indicative of the error in the solution.

$$\zeta = \frac{\tilde{d}_{rms}}{d_{rms}}$$

8. Repeat steps 2 to 7 until a target normalised RMS residual ζ_{target} is reached i.e when $\zeta < \zeta_{target}$.

A relaxation factor ψ can be used to assist convergence. For step 2, the solution becomes $\tilde{x}^n = \psi [\mathbb{A}^{nn}]^{-1} \tilde{d}^n$ and for step 4, $\tilde{d}^n = (1 - \psi)\tilde{d}^n$. For systems with solutions that do not converge, under-relaxation ($\psi < 1$) can improve convergence. However, for systems with solutions that do converge, over-relaxation ($\psi > 1$) can be used to preempt errors caused on each iteration and improve the speed of convergence.

3.2.3 Validation, Verification and Parameter Selection

MFS Verification

To verify the MFS code and demonstrate that the physical model is correct, the MFS was performed on a single sphere using a large number of nodes ($\mathcal{N} = 480$). This is comparable to using an extra fine mesh in CFD methods. The result can be compared to analytical results for a single sphere in Stokes flow - this analytical solution is known as Stokes Law (Stokes et al., 1851).

$$\mathbf{F} = -6\pi\mu\mathbf{u}d \quad (2.7)$$

Eq. 2.7 can be non-dimensionalized using a characteristic length scale L , the dynamic viscosity of the fluid μ and the particle density ρ . The non-dimensionalized velocity $\hat{\mathbf{U}}$ and force $\hat{\mathbf{F}}$ are given by,

$$\hat{\mathbf{U}} = \frac{L\rho}{\mu}\mathbf{u} \quad (3.11)$$

$$\hat{\mathbf{F}} = \frac{\rho}{\mu^2}\mathbf{F} \quad (3.12)$$

By letting $d = L$ and substituting Eqs. 3.11, 3.12 into Eq. 2.7,

$$\hat{\mathbf{F}} = -6\pi\mu\hat{\mathbf{U}} \quad (3.13)$$

Eq. 3.13 can be simplified further by letting $L, \rho, \mu = 1$ and the non-dimensionalized drag equation becomes,

$$\hat{\mathbf{F}} = -6\pi \quad (3.14)$$

The error ϵ in the calculated drag force in comparison to the analytical drag can be used to verify the MFS - both drag forces are non-dimensionalised (Lockerby and Collyer, 2016).

$$\epsilon = \left| \frac{\hat{\mathbf{F}}_{MFS} - \hat{\mathbf{F}}_{Analytical}}{\hat{\mathbf{F}}_{Analytical}} \right| \quad (3.15)$$

Using a high number of nodes ($\mathcal{N} = 480$), the error for MFS in calculating drag on a single sphere is $\epsilon = 7.29 \times 10^{-10}$, which demonstrates the method is highly accurate.

Number of Nodes

Fig. 3.6 demonstrates the effect of increasing the number of nodes on the error and processing time.

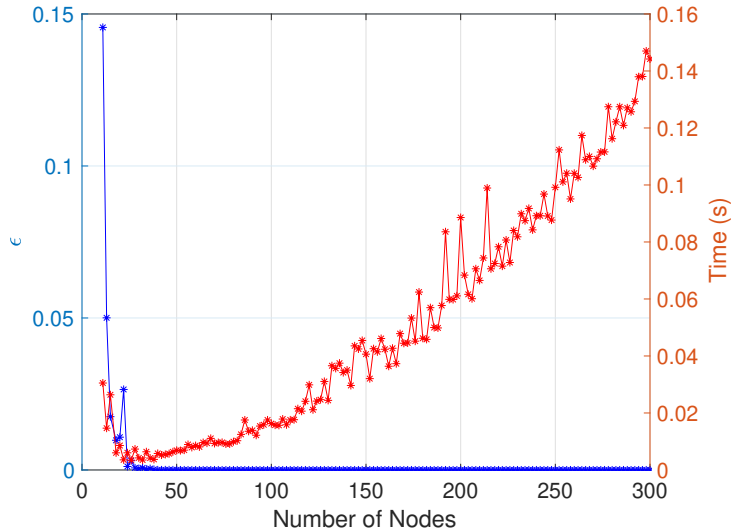


Figure 3.6: Number of nodes against error and processing time.

As the number of nodes increases, the accuracy of the drag also increases. However, this is at the expense of processing time since the number of simultaneous equations increases and matrix inversion becomes more computationally costly. $\mathcal{N} = 55$ appears to be an appropriate selection for the number of nodes when simulating a single sphere since $\epsilon \approx 0$ and the processing time is relatively low.

Ratio of Sites to Nodes

A condition of the MFS is that $\mathcal{M} \leq \mathcal{N}$ otherwise the system is underdetermined - the number of sites (\mathcal{M}) must be fewer than or equal to the number of nodes (\mathcal{N}). The standard MFS method uses $\mathcal{M} = \mathcal{N}$, however, the least squares MFS method uses an overdetermined system with $\mathcal{M} < \mathcal{N}$. The overdetermined system results in an increase in both accuracy and conditioning. However, as the ratio $\frac{\mathcal{M}}{\mathcal{N}}$ for the overdetermined system decreases, the marginal improvements also decrease. The only consequence of using the least squares method is that it is more computationally costly than the standard method (Cheng and Hong, 2020). The choice for the project was to use a slightly overdetermined system ($\frac{\mathcal{M}}{\mathcal{N}} = 0.8$), as the improvements in accuracy and stability of the solution outweighed the cost.

Distribution of Sites

The positioning of the sites can significantly affect convergence and accuracy since not all distributions guarantee that \mathbb{A} is invertible. The ability to choose the positioning of the sites can be an advantage of MFS if the site positions are selected carefully.

If sites are too close to each other, the equations become too similar and the matrix becomes near singular. One common approach is to place the sites on a ‘pseudo-boundary’ of a scaled version of the particle boundary; see Fig. 3.7 (Cheng and Hong, 2020).

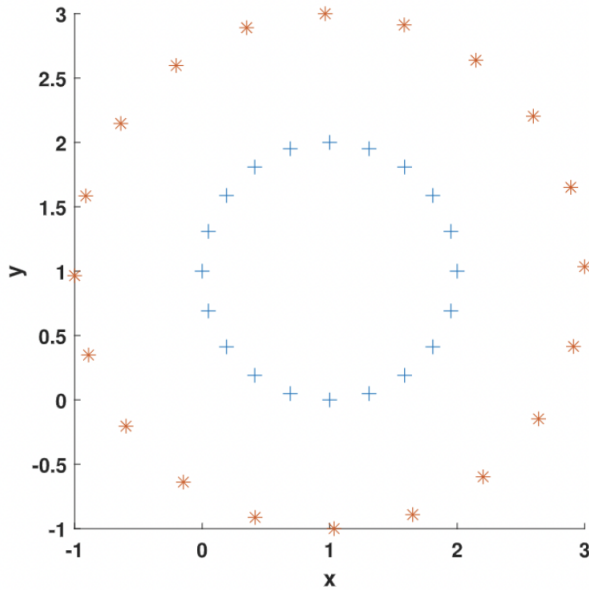


Figure 3.7: Distribution of sites on a circular disk (Cheng and Hong, 2020).

This approach was implemented in the MFS code where the sites are uniformly distributed on a scaled down sphere. Theoretically, as the radial distance between the pseudo-boundary and the particle boundary increases, the error exponentially decreases. However, in practice the distance has a limit as the MFS becomes ill-conditioned and error begins to increase as the distance becomes too large (Karageorghis, 2009). As a result, there is an optimal location for the pseudo-boundary where the error is minimised. This optimal placement occurs when the surface of the pseudo-boundary has a radius of approximately 0.2 for a spherule of radius 1 (Lockyer and Collyer, 2016).

Target Residual

The accuracy of the solution is dependent on the ratio of RMS values for the residual velocity at the boundary nodes \tilde{d}_{rms} and the actual velocity at the boundary nodes d_{rms} .

$$\zeta = \frac{\tilde{d}_{rms}}{d_{rms}}$$

If the scheme converges, \tilde{d}_{rms} and consequently ζ decrease towards zero for each subsequent iteration. The trade-off of improving accuracy is an increase in computational cost and processing time. For a higher number of iterations of the geometry, the processing time becomes exponentially large, so

the selection of an appropriate ζ is important.

ζ	No. Iterations	Time (s)
10^{-1}	3	0.26
10^{-2}	13	0.61
10^{-3}	27	1.08
10^{-4}	43	1.65
10^{-5}	61	2.39
10^{-6}	78	3.05
10^{-7}	96	3.64
10^{-8}	113	4.46
10^{-9}	130	5.10
10^{-10}	148	5.88

Table 3.1: Effect of ζ on the convergence of MFS for a fractal (Vicsek fractal, Iteration 3).

$\zeta = 10^{-4}$ was chosen for the project as the error remains minimal despite having a relatively fast processing time (Table. 3.1).

Relaxation Factor

As mentioned in Section 3.2.2, a relaxation factor ψ can be applied to the algorithm. Assuming that the scheme converges, over-relaxation ($\psi > 1$) speeds up convergence; however, this is dependent on the distribution of spherules. The effect of relaxation factor on convergence is demonstrated on a chain of 15 touching spheres in Fig. 3.8.

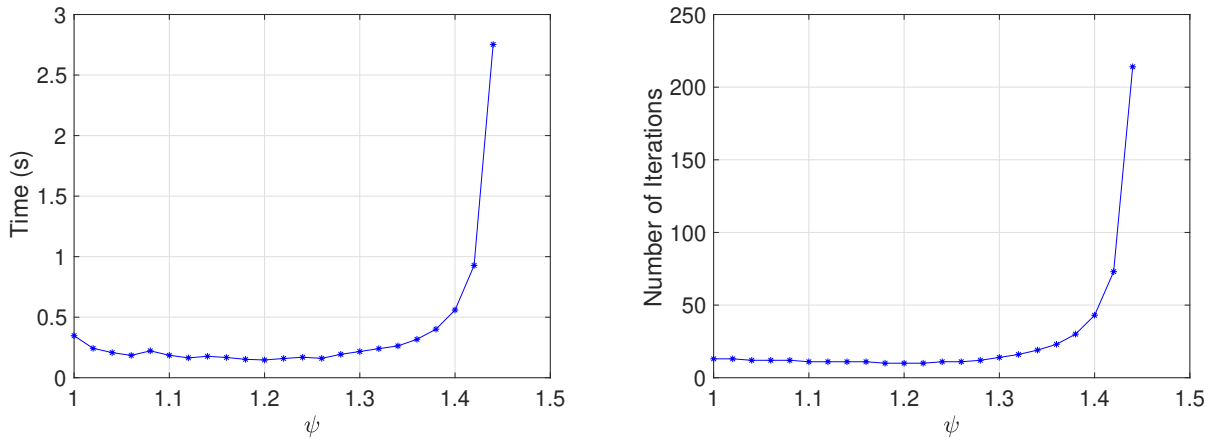
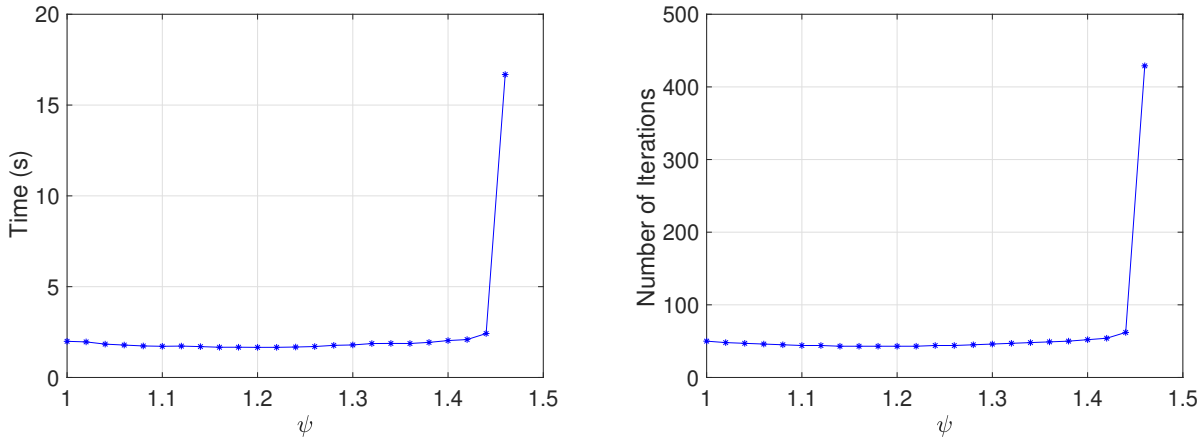


Figure 3.8: Effect of relaxation factor on the convergence of MFS for a chain of 15 touching spheres.

As expected, Fig. 3.8 shows that the processing time is dependent on the number of iterations

required for the solution to converge. The relaxation factor that resulted in the fastest convergence with the fewest number of iterations was $\psi \approx 1.2$. A noteworthy result is that there was a significant decrease in the rate of convergence for $\psi > 1.4$. For $\psi > 1.44$, the scheme no longer converged. This is due to the relaxation factor over-accounting for the Stokeslet velocity fields produced by forces at sites in neighbouring particles.



(a) Time against relaxation factor for a fractal (Vicsek fractal, Iteration 3). (b) Number of iterations against relaxation factor for a fractal (Vicsek fractal, Iteration 3).

Figure 3.9: Effect of relaxation factor on the convergence of MFS for a fractal (Vicsek fractal, Iteration 3).

Like the chain of touching spheres, for a fractal convergence was the fastest for $\psi \approx 1.2$; see Fig. 3.9. Due to this, $\psi = 1.2$ was used as the relaxation factor for all fractals. This was adjusted accordingly for each geometry in the case that the scheme did not converge. It is also noteworthy that there was a significant decrease in the rate of convergence for $\psi > 1.44$ and the scheme did not converge for $\psi > 1.46$.

Cutoff

The aforementioned MOR (Section 3.2.2) evaluates the individual effect of the force at each singularity site of particle n on the velocity of the fluid at each boundary node on the neighbouring particles $m = 1, 2 \dots P$ ($m \neq n$). To decrease processing time, a ‘cutoff’ can be utilised. When the distance between the centres of two particles exceeds this cutoff, instead of considering the individual effects of the point forces at each singularity site of particle n , these forces are replaced by a point force acting at the centre of n with the same magnitude as the resultant force of all singularity sites in the n_{th} particle.

The error ϵ in the calculated drag force when a cutoff is used $\hat{\mathbf{F}}_{cutoff}$ in comparison to the calculated drag force with no cutoff $\hat{\mathbf{F}}_\infty$ can be evaluated using Eq. 3.16.

$$\epsilon = \left| \frac{\hat{\mathbf{F}}_{cutoff} - \hat{\mathbf{F}}_\infty}{\hat{\mathbf{F}}_\infty} \right| \quad (3.16)$$

Using Eq. 3.16, the error and processing time were determined for a range of cutoff values for the Vicsek fractal. A cutoff of 1 refers to a distance of 1 sphere radius (1 unit).

Cutoff	ϵ	Time (s)
1	2.7×10^{-2}	0.28
3	-	-
5	7.0×10^{-3}	0.67
7	6.0×10^{-3}	0.92
9	3.2×10^{-3}	1.31
11	2.5×10^{-3}	1.56
13	5.6×10^{-4}	1.71
15	1.2×10^{-4}	1.82
∞	0	1.82

Table 3.2: Effect of cutoff on error and processing time of MFS for a fractal (Vicsek fractal, Iteration 3).

A cutoff value of 5 was selected as the error is minimal despite a significant reduction in processing time (Table. 3.2). For larger fractals, this reduction in processing time is amplified.

Chapter 4

Results and Analysis

The primary aim of the project was to investigate the relationship between drag and the number of monomers in the aggregate. Chapter 3 details how the MOR can be used to numerically simulate Stokes flow around an aggregate. In Section 3.2.3, the final parameters selected for the MOR were:

- $\mathcal{N} = 55$ nodes on each primary particle
- a ratio of sites to nodes of $\frac{\mathcal{M}}{\mathcal{N}} = 0.8$
- sites distributed on the surface of a spherical pseudo-boundary of radius 0.2
- a target RMS residual error of $\zeta = 10^{-4}$
- a relaxation factor $\psi = 1.2$
- a cutoff value of 5

All drag results were non-dimensionalised and divided by Stokes drag i.e. $F_{Drag} = \left| \hat{\mathbf{F}}_{Drag} \right| = \frac{\hat{\mathbf{F}}_{MOR}}{6\pi}$ in order to determine drag relative to a single sphere. For the simulations, a translational flow was used with a unit magnitude in the flow direction $|\mathbf{u}| = 1$.

4.1 Integer Dimension Aggregates

Before evaluating the trends found in fractal aggregates, drag was calculated for aggregates of integer dimension - a chain and a square. Drag on aggregates of formed of self-similar clusters of spheres was later calculated for comparison.

4.1.1 Chain

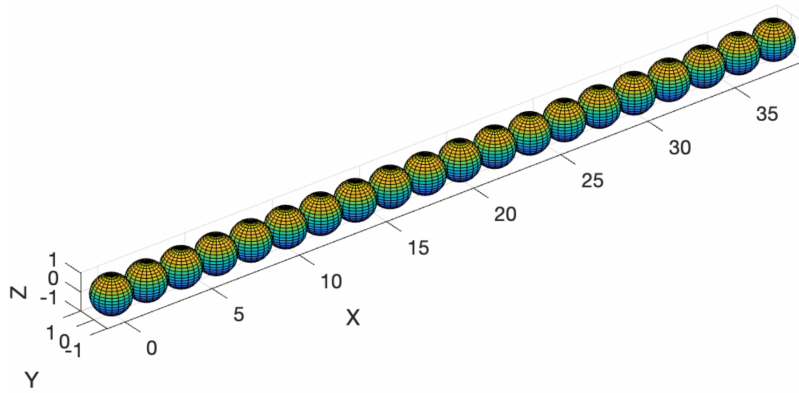


Figure 4.1: Chain extending in the x-direction.

The first aggregate that was investigated was a chain of touching spheres extending in the x-direction (Fig. 4.1), which has a dimension of $D_f = 1$.

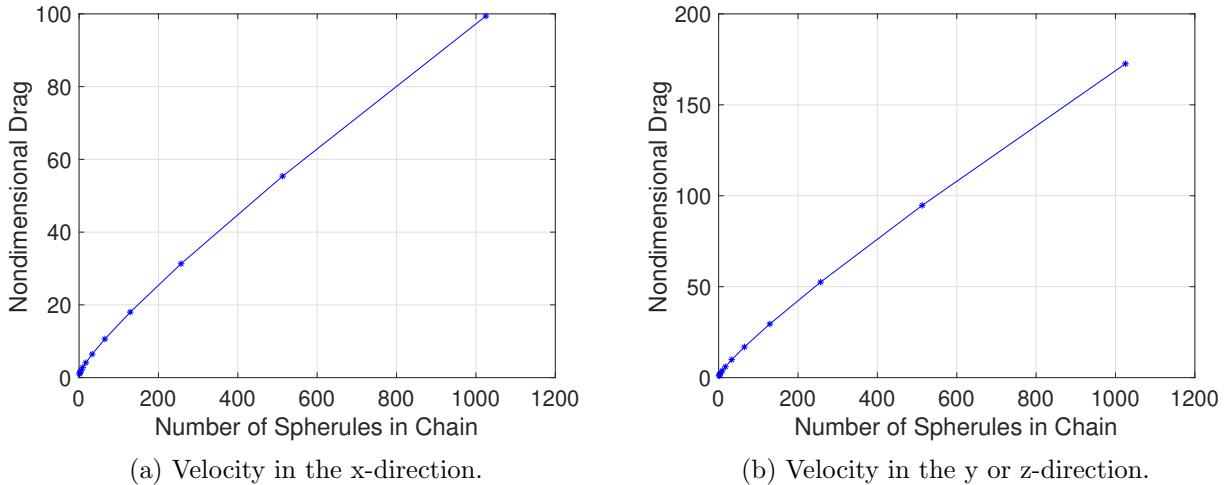


Figure 4.2: Drag versus number of spherules in a chain extending in the x-direction.

Fig. 4.2 shows the drag on the chain for a range of chain lengths - implied by the number of spherules in the chain. A unit velocity applied in both the y and z directions is hydrodynamically equivalent so there were two cases to calculate the drag for - flow parallel to the chain (Fig. 4.2a) and flow perpendicular to the chain (Fig. 4.2b). Since the plot is not linear, a loglog plot for this data was produced to determine the plausibility of a power law fit.

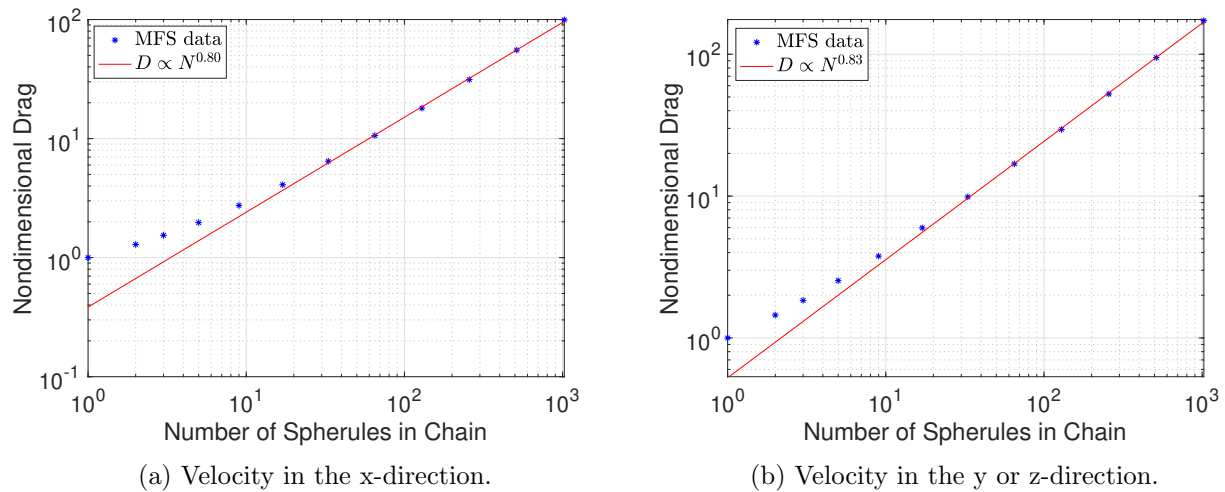


Figure 4.3: Drag versus number of spherules in a chain extending in the x-direction on loglog plots with fitted curves.

In Fig. 4.3 the last 6 data points were used to determine the line of best fit. Although the data is not linear on the loglog plot when the number of spherules is low, it appears to become linear as the number increases. Dimensional arguments suggest that as the number of spherules in the chain increases, the dimensions of the individual spherules become negligible in comparison to the length of the chain. Effectively, the chain can be treated as a 1D line. The equations for the lines of best fit for velocity in the x, y and z-directions are, $D_x = 0.38N^{0.80}$ and $D_{yz} = 0.52N^{0.83}$ where N is the number of spherules in the chain. A noteworthy result for the chain is that the drag was smaller in Fig. 4.3a than Fig. 4.3b. This is due to a shielding effect that occurs when the chain extends in the same direction as velocity.

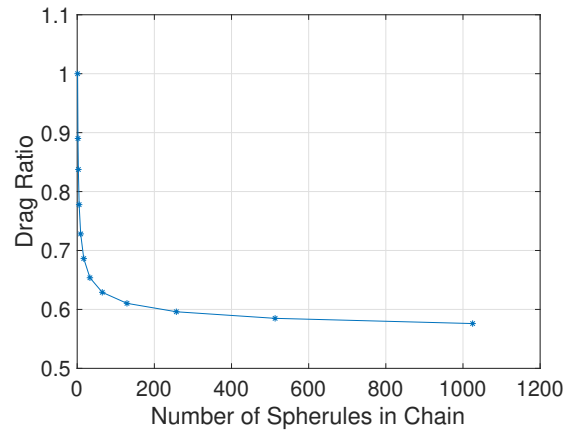


Figure 4.4: Drag ratio versus number of spherules in a chain.

Fig. 4.4 shows the drag ratio $\frac{D_x}{D_{yz}}$ approaches a constant as $N \rightarrow \infty$.

4.1.2 Square

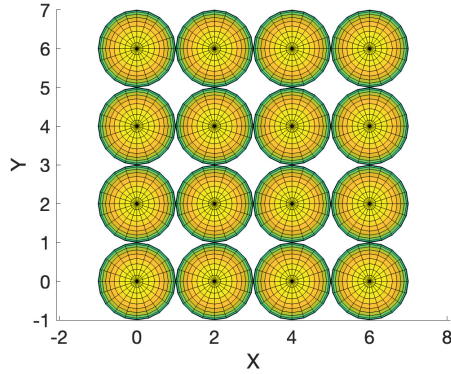


Figure 4.5: Square in the x-y plane.

The most efficient packing of spheres in two-dimensional space is the square which as a result has a dimension $D_f = 2$.

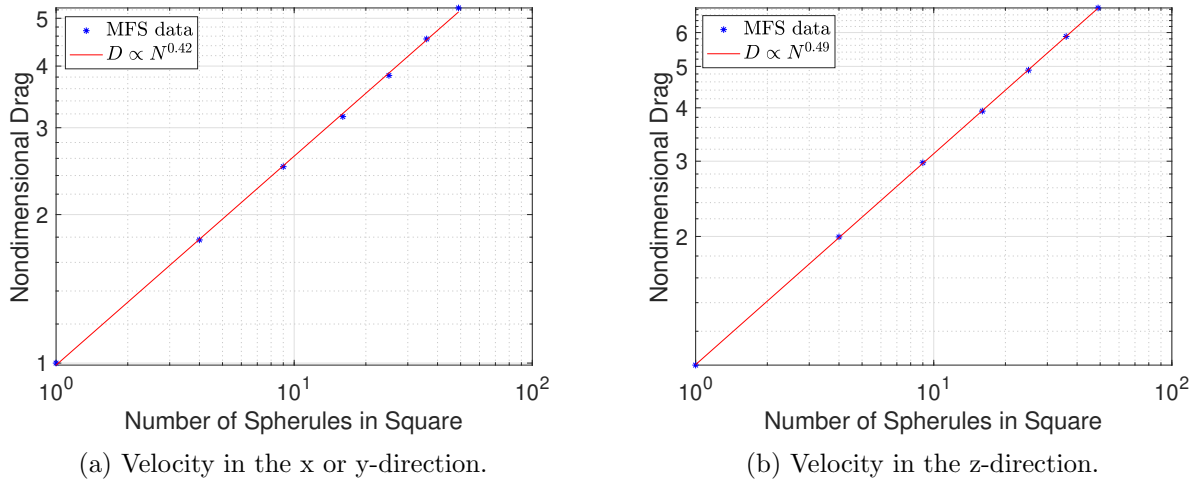


Figure 4.6: Drag versus number of spherules in a square in the x-y plane on loglog plots with fitted curves.

For a square in the x-y plane (Fig. 4.5), the drag was plotted against the number of spherules within the square in Fig. 4.6, which has a dimension of $D_f = 2$. The equations for the lines of best fit for velocity in the x, y and z-directions are $D_{xy} = 0.99N^{0.42}$ and $D_z = 1.00N^{0.49}$. $D_z \propto N^{\frac{1}{2}}$ appears to be a good fit for the data which is significant since $\frac{1}{2} = \frac{1}{D_f}$.

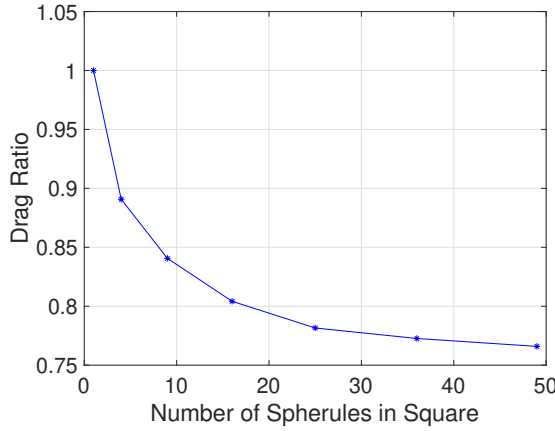


Figure 4.7: Drag ratio versus number of spherules in a square.

The drag ratio $\frac{D_{xy}}{D_z}$ is plotted in Fig. 4.7. Similar to a chain, it appears that the drag ratio approaches a constant as $N \rightarrow \infty$.

4.2 2D Fractal Aggregates

Flow was simulated around a range of common 2D aggregates in the x-y plane. Although they were formed using spherical particles, as the overall size of the aggregate increases, the thickness of the aggregate becomes negligible. Since 2D fractals are restricted to one plane, this has a computational advantage in that since the first unit has a small number of particles, the number of iterations that the flow could be simulated for in a given time was higher than for 3D. This resulted in a larger amount of data being collected for 2D fractals than for 3D.

4.2.1 Vicsek Fractal

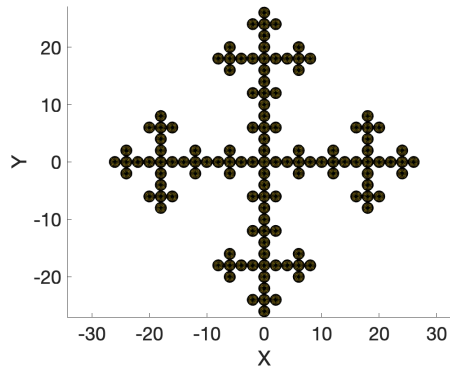
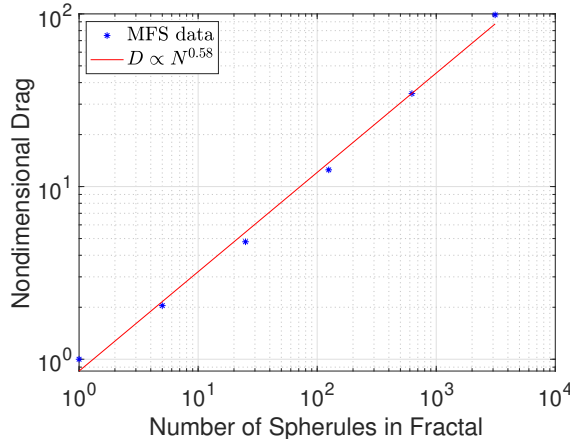
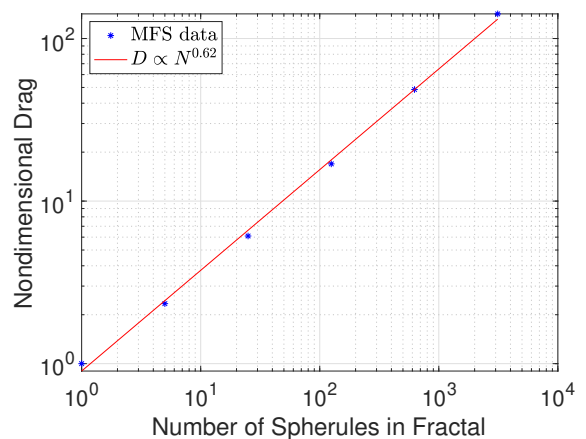


Figure 4.8: Vicsek fractal in the x-y plane.

The first of the 2D fractal aggregates was the Vicsek fractal in Fig. 4.8, which has a fractal dimension of $D_f = 1.47$ (or $\frac{1}{D_f} = 0.68$). The main application of this particular fractal is as a compact antenna as due to its fractal dimension, it has no area but an infinite perimeter. As a result, it can be used as a fractal antenna to maximise its effective length to receive or transmit EM waves (Fuqi et al., 2004).



(a) Velocity in the x or y-direction.



(b) Velocity in the z-direction.

Figure 4.9: Drag versus number of spherules in the Vicsek fractal in the x-y plane on loglog plots with fitted curves.

For the fractal in the x-y plane (Fig. 4.8), the drag was plotted against the number of spherules within the fractal in Fig. 4.9. The equations for the lines of best fit for velocity in the x, y and z-directions are $D_{xy} = 0.85N^{0.58}$ and $D_z = 0.90N^{0.62}$.

4.2.2 Sierpinski Triangle Fractal

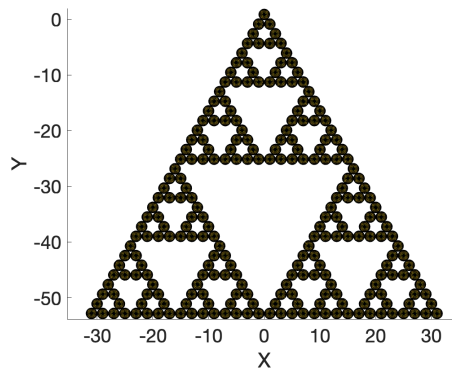
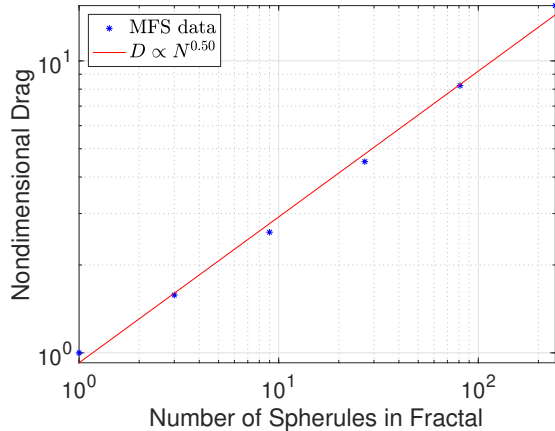
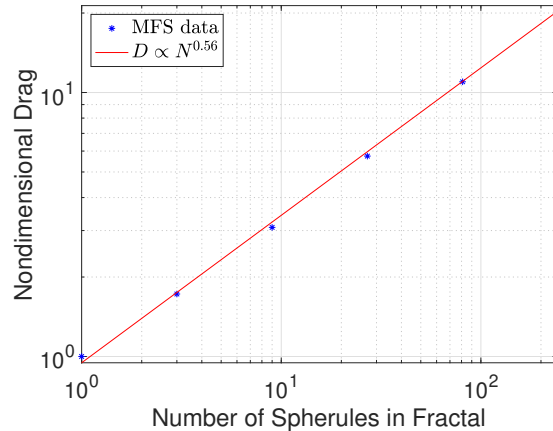


Figure 4.10: Sierpinski triangle in the x-y plane.

The second of the 2D fractal aggregates was the Sierpinski triangle (Fig. 4.10). This has a fractal dimension of $D_f \approx 1.59$ (or $\frac{1}{D_f} \approx 0.63$). As one of the most common fractals, it makes the Sierpinski triangle an obvious geometry to examine.



(a) Velocity in the x or y-direction.



(b) Velocity in the z-direction.

Figure 4.11: Drag versus number of spherules in a 2D-fractal in the x-y plane on loglog plots with fitted curves.

For the fractal in the x-y plane (Fig. 4.10), the drag was plotted against the number of spherules within the fractal in Fig. 4.11. The equations for the lines of best fit for velocity in the x, y and z-directions are $D_{xy} = 0.92N^{0.5}$ and $D_z = 0.95N^{0.56}$. Like both the square and the Vicsek fractal, the Sierpinski triangle experiences the same drag for velocity in both the x and y directions which was unexpected.

4.2.3 Sierpinski Triangle Fractal - 2

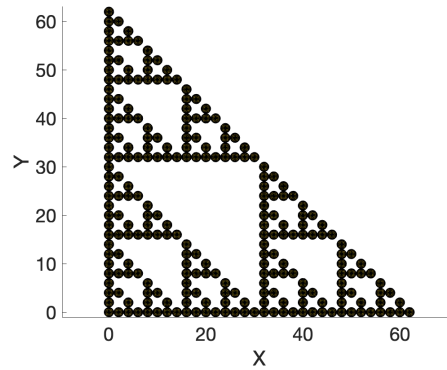


Figure 4.12: 2D-fractal in the x-y plane.

The next aggregate that was investigated was another Sierpinski triangle (Fig. 4.12). Unlike the Sierpinski triangle in Fig. 4.10, which uses an equilateral triangle arrangement for the first unit, this aggregate uses a right-angled triangle arrangement. Since the aggregate has an initial unit consisting of 3 spherules, it also has a fractal dimension of $D_f \approx 1.59$ (or $\frac{1}{D_f} \approx 0.63$).

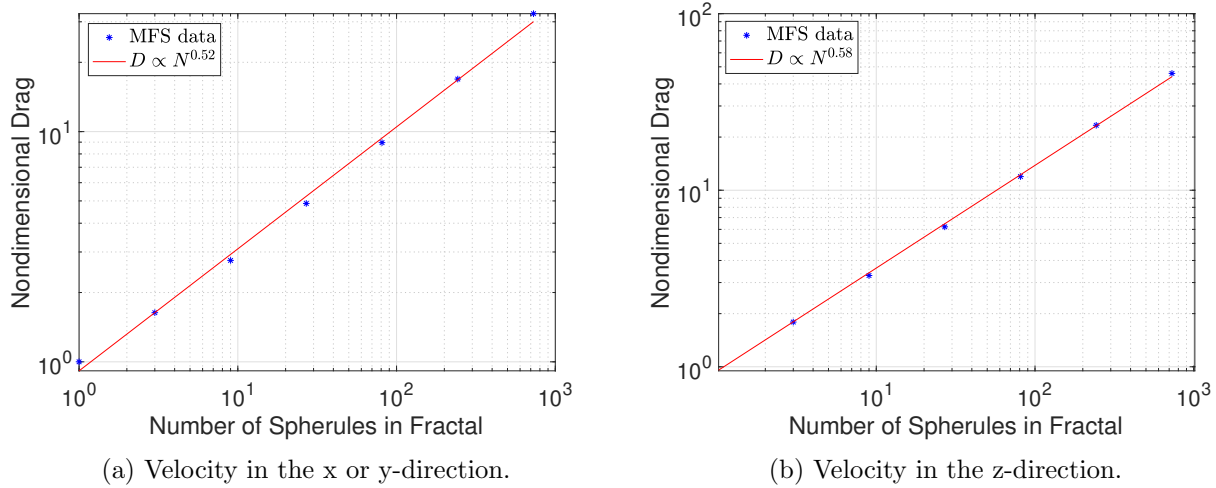


Figure 4.13: Drag versus number of spherules in a 2D-fractal in the x-y plane on loglog plots with fitted curves.

For the fractal in the x-y plane (Fig. 4.12), the drag was plotted against the number of spherules within the fractal in Fig. 4.13. The equations for the lines of best fit for velocity in the x, y and z-directions are $D_{xy} = 0.91N^{0.53}$ and $D_z = 0.95N^{0.58}$.

4.3 3D Fractal Aggregates

The 3D aggregates that were investigated were 3D analogues of the 2D aggregates. These aggregates are more similar to fractal aggregates observed in nature as they are not restricted to a single plane. The disadvantage of simulating the 3D aggregates was the significant increase in processing time in comparison to 2D aggregates.

4.3.1 3D Vicsek Fractal

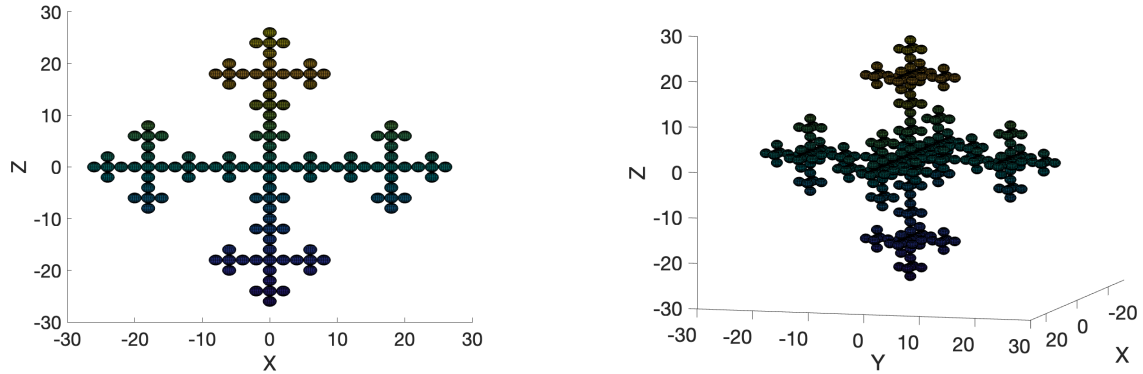


Figure 4.14: 3D fractal.

The first of the 3D aggregates was the 3D analogue of the Vicsek fractal (Fig. 4.14), which has a fractal dimension of $D_f \approx 1.77$ (or $\frac{1}{D_f} \approx 0.56$). This was perhaps the most interesting aggregate as it most closely resembles a snowflake, and its application to nature is more obvious.

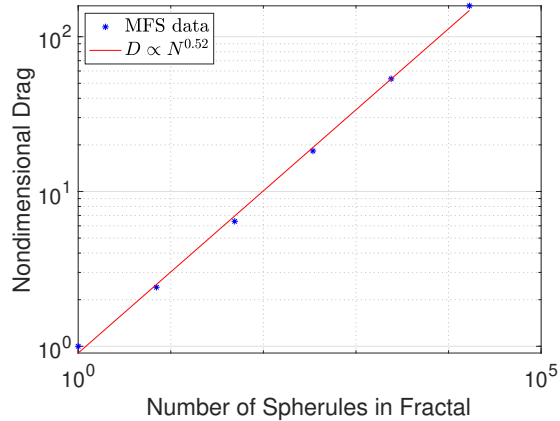


Figure 4.15: Drag versus number of spherules in a fractal on a loglog plot with a fitted curve.

For the 3D Vicsek fractal, the drag was plotted against the number of spherules within the fractal in Fig. 4.15. The equation for the line of best fit is $D_{XYZ} = 0.90N^{0.52}$. Due to the rotational symmetry, the drag experienced in all directions is equal.

4.3.2 Sierpinski Tetrahedron Fractal

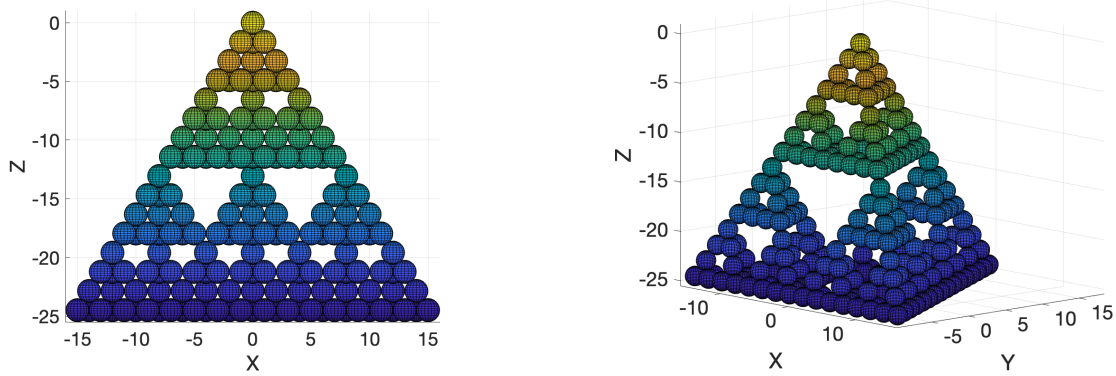


Figure 4.16: Sierpinski tetrahedron.

The second of the 3D fractal aggregates was the Sierpinski tetrahedron (Fig. 4.16) which has a dimension of $D_f = 2$ (or $\frac{1}{D_f} = 0.5$). This is a surprising result since despite being a fractal aggregate, the Hausdorff dimension is non-fractal. It still possesses a fractal nature however since its Hausdorff dimension is less than the 3 dimensions of space that it occupies.

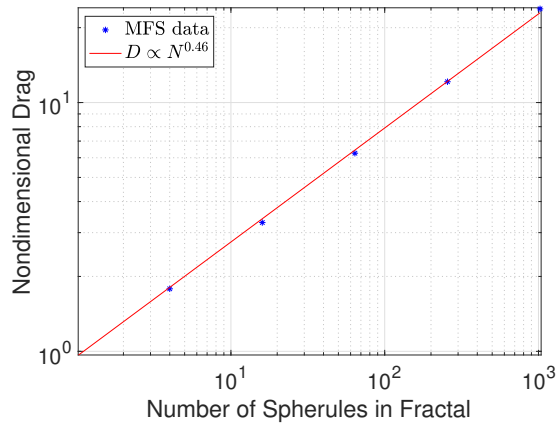


Figure 4.17: Drag versus number of spherules in a fractal on a loglog plot with a fitted curve.

For the Sierpinski Tetrahedron, the drag was plotted against the number of spherules within the fractal in Fig. 4.17. The drag for velocities in all directions was once again identical, so the equation for the line of best fit is $D_{XYZ} = 0.96N^{0.46}$. This is another unexpected result but it is equivalent to the Sierpinski triangle, which experienced the same drag in both the x and y directions.

4.3.3 Sierpinski Tetrahedron Fractal - 2

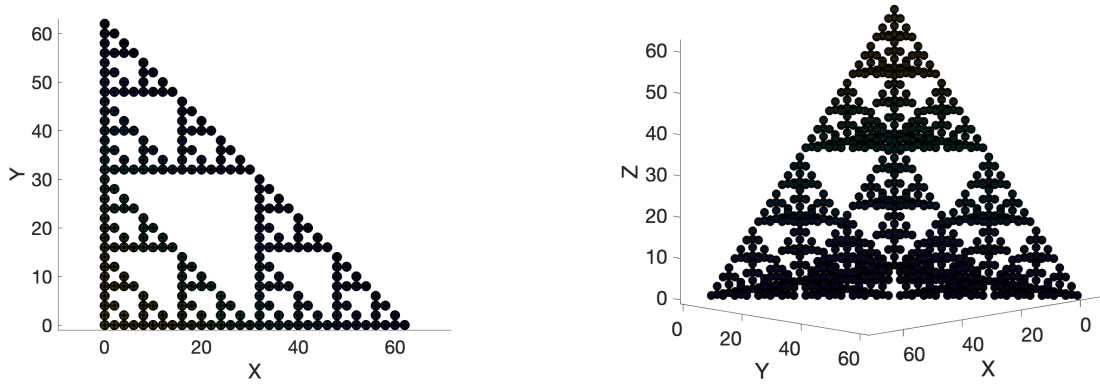


Figure 4.18: 3D fractal.

The final 3D aggregate was another Sierpinski tetrahedron (Fig. 4.18) which also has a dimension of $D_f = 2$ (or $\frac{1}{D_f} = 0.5$). Unlike the previous Sierpinski tetrahedron, this is a trirectangular tetrahedron where all three faces meet at right angles at one vertex.

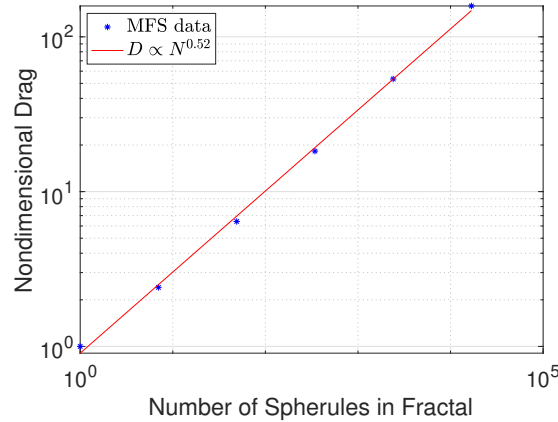


Figure 4.19: Drag versus number of spherules in a fractal on a loglog plot with a fitted curve.

For the final aggregate, the drag was plotted against the number of spherules within the fractal in Fig. 4.19. Once again, the drag calculated for velocities in the x, y and z directions was the same. The equation for the line of best fit is $D_{XYZ} = 1.61N^{0.48}$.

Chapter 5

Discussion

The various trends that have arisen through analysis of the results were discussed in this section in further detail. The main observations were the power law relationship, the effect of symmetries on drag, and the drag ratio of 2D fractal aggregates.

5.1 Power Law Relationship

The most significant observation was the power-law relationship that exists between the drag on an aggregate and the number of monomers it consists of. As demonstrated by the linear fits on the loglog plots for both 2D and 3D fractals in Chapter 4, the relationship is of the form,

$$F_{Drag} = kN^x \quad (5.1)$$

where F_{Drag} is the magnitude of the drag force, k is the scaling prefactor, N is the number of monomers and x is the drag-mass scaling exponent. The relationship does not hold particularly well for low N , however as $N \rightarrow \infty$, x approaches a limit.

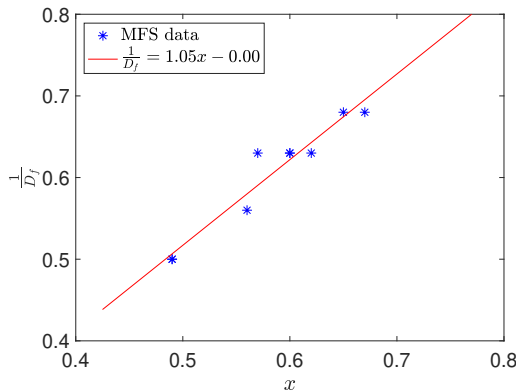


Figure 5.1: $\frac{1}{D_f}$ against x for the large aggregate case.

This scaling exponent in the limiting case of a large aggregate is evaluated in Fig. 5.1. This does not appear to apply to the linear chain of spheres; however, since this is not a fractal aggregate it can be neglected (Sorensen, 2011). To determine x , the exponent was calculated using the last two data points for each fractal. These scaling exponents were plotted against the fractal dimension for all 2D and 3D aggregates in Fig. 5.1. The line of best fit for the data is $\frac{1}{D_f} = 1.05x + 0.00$. This indicates that as $N \rightarrow \infty$, $x \rightarrow \frac{1}{D_f}$. The nondimensional drag on a self-similar aggregate (relative to a single sphere) is only a function of the number of spherules in the aggregate and its fractal dimension. This confirms the hypothesis Eq. 2.17.

5.2 Symmetry

For the 2D aggregates, the drag was identical for velocities applied in both x and y-directions. This was unexpected for the Sierpinski triangle and Sierpinski triangle - 2 since the structure is different for both directions. This was also observed for all 3D fractals where regardless of the direction of the applied velocity, the drag was identical.

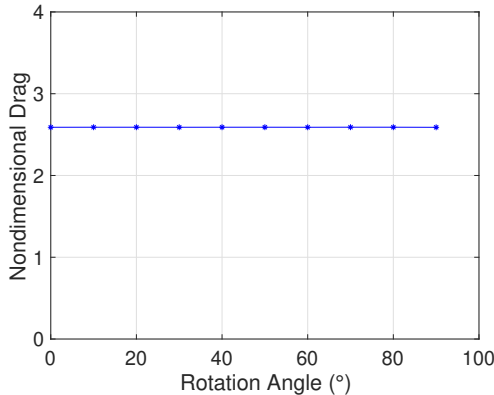


Figure 5.2: Drag against rotation angle for the Sierpinski fractal (Iteration 3).

The effect of rotation angle on the drag experienced by a fractal was investigated for the third iteration of the Sierpinski triangle in Fig. 5.2 by applying a rotation matrix to the position vectors of the spherules. The drag experienced by the fractal is independent of the angle of the flow relative to the fractal aggregate. This can be explained through the resistance tensor \mathbb{R} in Eq. 5.2.

$$\mathbf{F} = \mathbb{R} \cdot \mathbf{u} \quad (5.2)$$

This resistance tensor is an intrinsic property of the geometry of interest and characterizes the resistance of a body to translational motion for low Re . Due to the symmetric property of the tensor, a 3D geometry has at least 3 mutually perpendicular axis such that if it moves parallel to one of them, it will only experience a force in the direction. If an object has a number of symmetries itself,

such as the Sierpinski triangle fractal, the resistance tensor becomes diagonal. The consequence of this is that regardless of the orientation the same force vector \mathbf{F} is produced (Brenner, 1963). For the 2D and 3D geometries that experienced the same drag regardless of orientation, the resistance matrices are of the form,

$$\mathbb{R}_{2D} = \begin{bmatrix} \mu & 0 & 0 \\ 0 & \mu & 0 \\ 0 & 0 & \alpha \end{bmatrix} \quad \text{and} \quad \mathbb{R}_{3D} = \begin{bmatrix} \mu & 0 & 0 \\ 0 & \mu & 0 \\ 0 & 0 & \mu \end{bmatrix}$$

5.3 Drag Ratio

It was observed that the drag was less when the flow was parallel to the plane of the fractal than for flow perpendicular to the fractal. It was initially observed for both a chain and a square that the ratio of the two drags approaches a constant as $N \rightarrow \infty$. This result was reproduced when plotting the drag ratio for the various fractal geometries in Appendix B. This is indicative of the aforementioned drag-mass scaling exponent x approaching a constant at high N .

The reduced drag in the parallel direction is due to a shielding effect whereby the central particles within the aggregates interact less strongly with the flow (Leichtberg et al., 1976). This effect is visualised using streamlines in Appendix C.

Chapter 6

Conclusions and Recommendations for Further Work

Through numerical simulations using MFS and MOR, a power law relationship between the drag on a self-similar fractal and the number of primary particles in the fractal was derived. As the number of primary particles become asymptotically large, the scaling exponent x approaches the reciprocal of the fractal dimension $\frac{1}{D_f}$ for the given fractal. Further work could examine the effect of the number of primary particles on the mobility radius or mobility ratio instead of the drag.

An additional finding is that for fractals that possess symmetries, the drag experienced by them is independent of their orientation. This is due to the diagonal nature of the resistance matrix for these particular fractals. As a result 2D fractals experienced equal drag for velocities in the same plane as the fractal and 3D fractals experienced equal drag in all orientations.

The final significant finding was that the ratio of drag on a fractal for velocities parallel to the plane of the fractal to the velocity perpendicular to the fractal, approached a constant at high N . This is also indicative of the exponent in the scaling law, mentioned above, approaching a constant.

A recommendation for further work is to extend research from self-similar fractals to self-affine fractals such as those in Appendix A. Unlike self-similar fractals that are invariant under isotropic changes of length scale, a self-affine fractal has more than one fractal dimension, so rescaling is not isotropic.

In regards to the formation of the basic structure of the aggregate, instead of aggregates formed of spherical primary particles, non-spherical particles could be used. Furthermore, instead of using touching spheres, fractals that have some spacing between particles could also be investigated.

The final recommendations relates to the simulation of the fluid itself. Instead of using a dilute suspension of aggregates, the pair-wise interaction of aggregates could be investigated. Also, this project restricts the type of flow to continuum flow. Self-similar fractals in other flow regimes such as the slip regime, transitional regime or the free molecular regime could also be investigated.

Bibliography

- Alves, C. J. (2009). On the choice of source points in the method of fundamental solutions. *Engineering Analysis with Boundary Elements*, 33(12):1348–1361.
- Brenner, H. (1963). The stokes resistance of an arbitrary particle. *Chemical Engineering Science*, 18(1):1–25.
- Cheng, A. H. and Hong, Y. (2020). An overview of the method of fundamental solutions—solvability, uniqueness, convergence, and stability. *Engineering analysis with boundary elements*, 120:118–152.
- Christensen, U. R. (2015). Iron snow dynamo models for ganymede. *Icarus*, 247:248–259.
- Fairweather, G. and Karageorghis, A. (1998). The method of fundamental solutions for elliptic boundary value problems. *Advances in Computational Mathematics*, 9:69–95.
- Falconer, K. (2004). *Fractal geometry: mathematical foundations and applications*. John Wiley & Sons.
- Fuqi, S., Hongming, G., and Baoxin, G. (2004). Analysis of a vicsek fractal patch antenna. In *ICMMT 4th International Conference on, Proceedings Microwave and Millimeter Wave Technology, 2004.*, pages 98–101. IEEE.
- Guazzelli, E. and Morris, J. F. (2011). *A physical introduction to suspension dynamics*, volume 45. Cambridge University Press.
- Heinson, W., Sorensen, C., and Chakrabarti, A. (2012). A three parameter description of the structure of diffusion limited cluster fractal aggregates. *Journal of colloid and interface science*, 375(1):65–69.
- Jungblut, S., Joswig, J.-O., and Eychmüller, A. (2019). Diffusion-and reaction-limited cluster aggregation revisited. *Physical Chemistry Chemical Physics*, 21(10):5723–5729.
- Karageorghis, A. (2009). A practical algorithm for determining the optimal pseudo-boundary in the method of fundamental solutions. *Adv. Appl. Math. Mech.*, 1(4):510–528.

- Leichtberg, S., Pfeffer, R., and Weinbaum, S. (1976). Stokes flow past finite coaxial clusters of spheres in a circular cylinder. *International Journal of Multiphase Flow*, 3(2):147–169.
- Lockerby, D. (2022a). Px921: Micro & nano flows across scales & phases.
- Lockerby, D. (2022b). Simulating creeping flow around a spatial distribution of particles: the method of fundamental solutions (mfs) and the method of reflections (mor).
- Lockerby, D. A. and Collyer, B. (2016). Fundamental solutions to moment equations for the simulation of microscale gas flows. *Journal of Fluid Mechanics*, 806:413–436.
- Luo, J., Zhang, Q., Zhang, C., Zhang, Y., and Chakrabarty, R. K. (2021). The fractal characteristics of atmospheric coated soot: Implication for morphological analysis. *Journal of Aerosol Science*, 157:105804.
- McCorquodale, M. W. and Westbrook, C. (2021). Trail: A novel approach for studying the aerodynamics of ice particles. *Quarterly Journal of the Royal Meteorological Society*, 147(734):589–604.
- Meakin, P. (1987). Fractal aggregates. *Advances in Colloid and Interface science*, 28:249–331.
- Sorensen, C. (2011). The mobility of fractal aggregates: a review. *Aerosol Science and Technology*, 45(7):765–779.
- Stokes, G. G. et al. (1851). On the effect of the internal friction of fluids on the motion of pendulums.
- Xu, N. and Fan, L. (2014). Numerical simulation of flow involving a fractal aggregate. *Journal of the Taiwan Institute of Chemical Engineers*, 45(4):1403–1410.
- Zhao, L. (2016). Streamlines in the symmetry plane for a uniform flow past a rigid sphere. The radius of the rigid sphere is $a=1$.

Appendix A

Self-Affine Fractals

The drag results for the self-affine fractals in Fig. A.1 and Fig. A.3 are plotted below.

A.1 2D Fractal-4

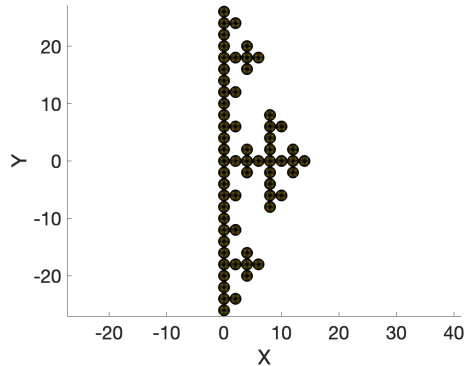


Figure A.1: 2D-fractal in the x-y plane.

For a fractal in the x-y plane (Fig. A.1), the drag was plotted against the number of spherules within the fractal in Fig. A.2.

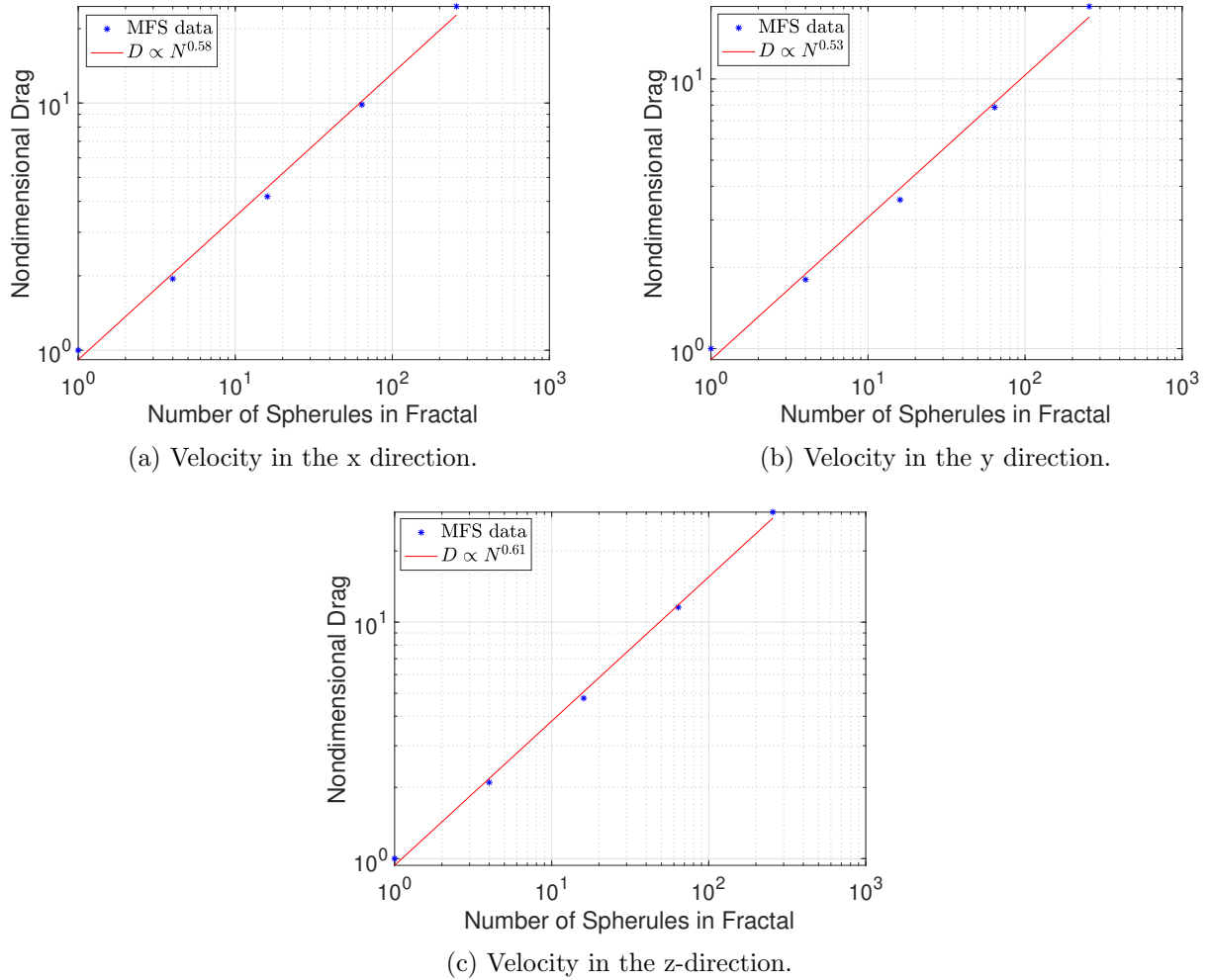


Figure A.2: Drag versus number of spherules in a 2D-fractal in the x-y plane on loglog plots with fitted curves.

The equations for the lines of best fit for velocity in the x, y and z-directions are $D_x = 0.92N^{0.58}$, $D_y = 0.91N^{0.53}$ and $D_z = 0.94N^{0.61}$.

A.2 3D Fractal-4

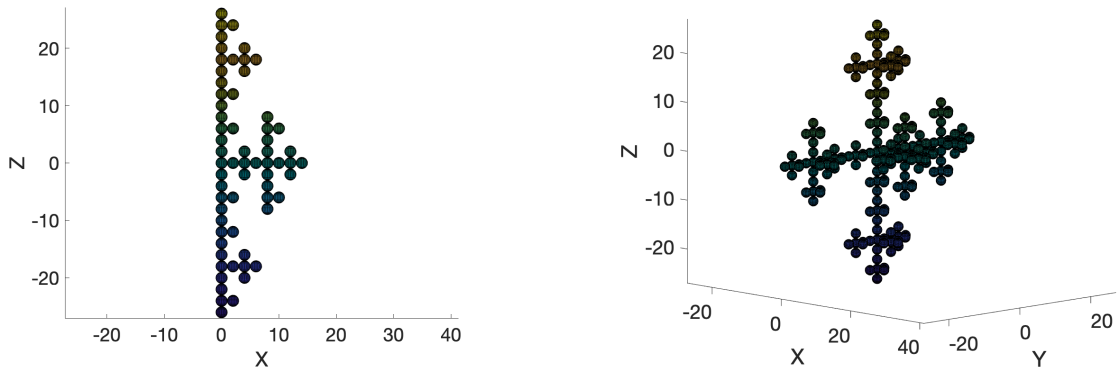


Figure A.3: 3D fractal.

For a 3D fractal (Fig. A.3), the drag was plotted against the number of spherules within the fractal in Fig. A.4.

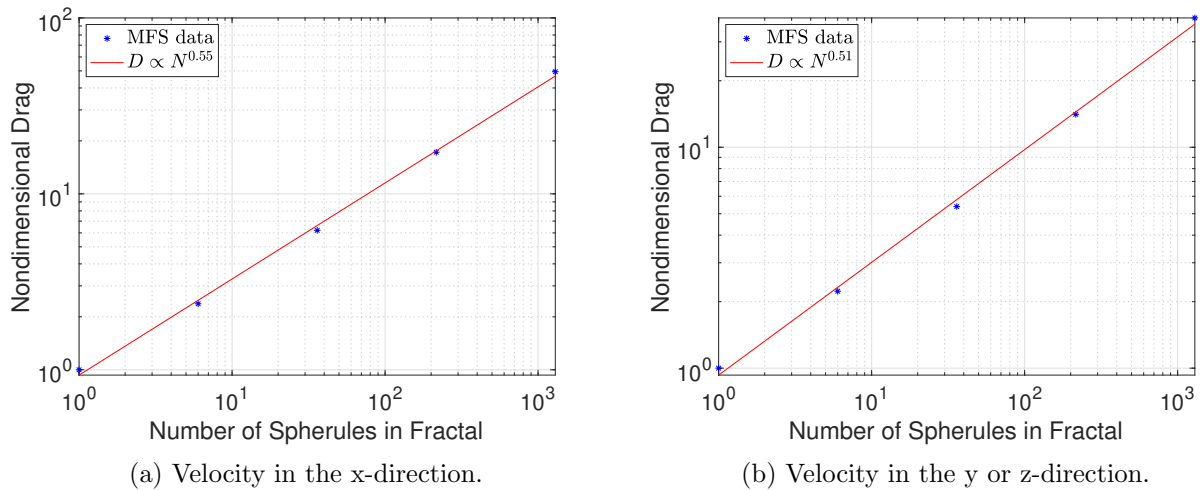


Figure A.4: Drag versus number of spherules in a fractal on a loglog plot with a fitted curve.

The equations for the lines of best fit for velocity in the x, y and z-directions are $D_x = 0.93N^{0.55}$ and $D_{yz} = 0.93N^{0.51}$.

Appendix B

Additional Drag Plots

B.1 Large Aggregates

In addition to the drag plots in Chapter 4, lines of best fit were generated using the last two data points for each fractal - referred to as the ‘Large N fit’ in the plots. These plots are useful since, at higher N , we observe that the scaling exponent approaches the reciprocal of the fractal’s Hausdorff dimension in asymptotically large aggregates where $N \rightarrow \infty$ (Sorensen, 2011) - referred to as ‘ $\frac{1}{D_f}$ Fit’ in plots. These plots are illustrated in Fig. B.1 - B.6.

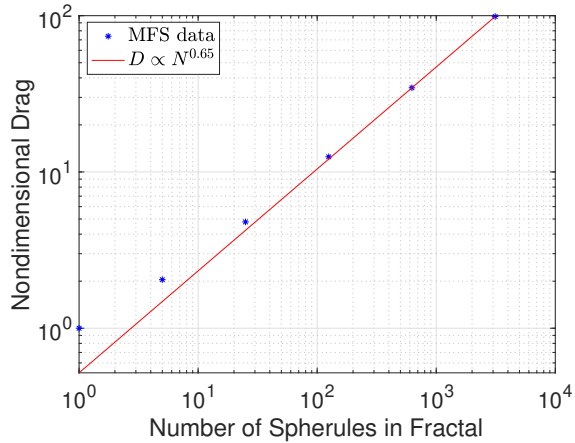
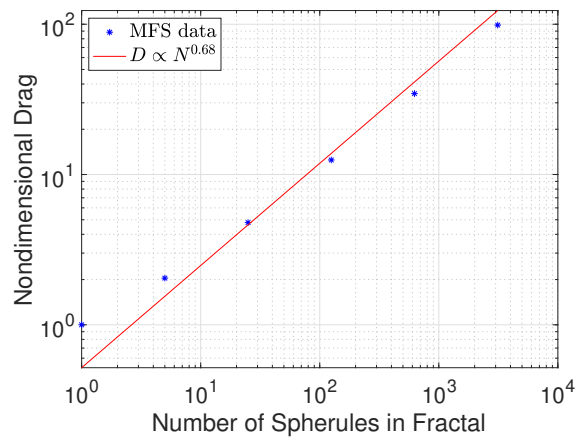
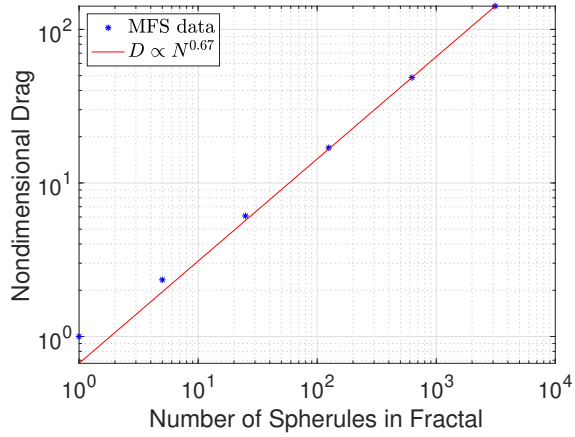
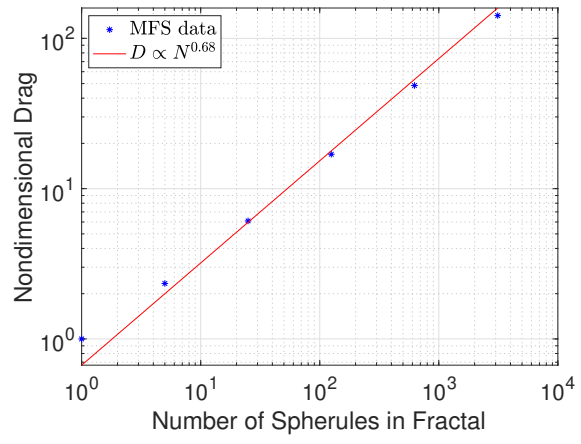
(a) Large N Fit: Velocity in the x direction.(b) $\frac{1}{D_f}$ Fit: Velocity in the x direction.(c) Large N Fit: Velocity in the z direction.(d) $\frac{1}{D_f}$ Fit: Velocity in the z direction.

Figure B.1: Drag versus number of spherules in the Vicsek fractal.

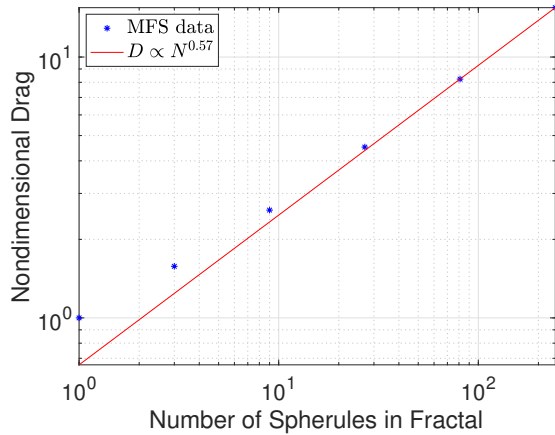
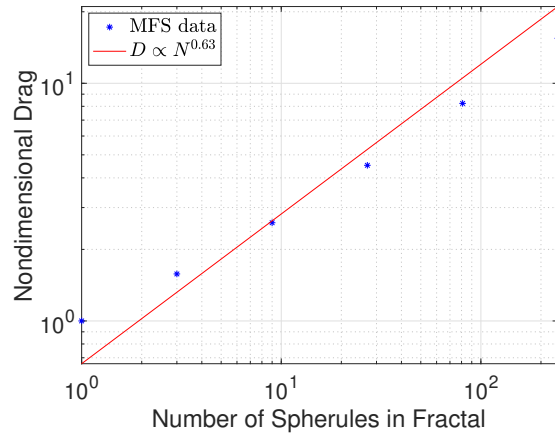
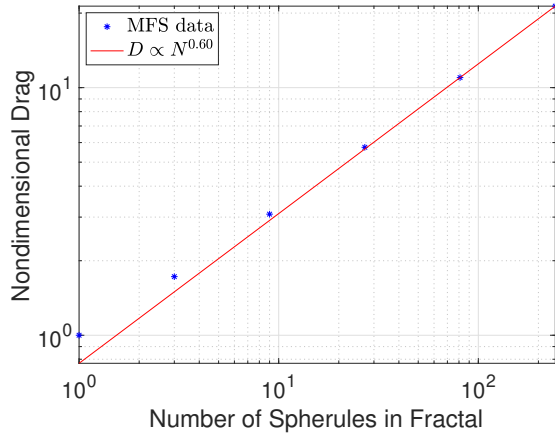
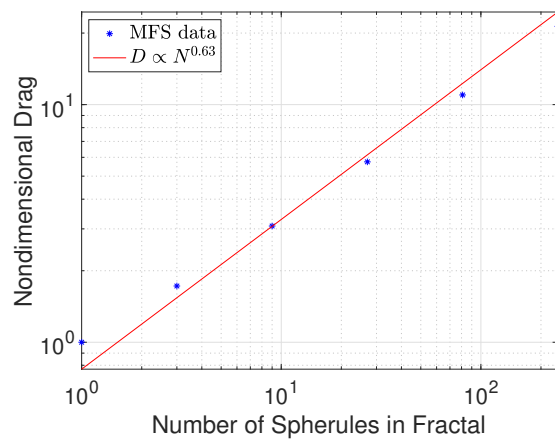
(a) Large N Fit: Velocity in the x direction.(b) $\frac{1}{D_f}$ Fit: Velocity in the x direction.(c) Large N Fit: Velocity in the z direction.(d) $\frac{1}{D_f}$ Fit: Velocity in the z direction.

Figure B.2: Drag versus number of spherules in the Sierpinski triangle fractal.

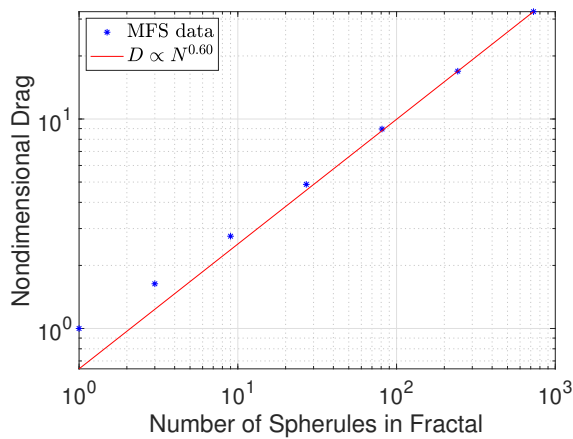
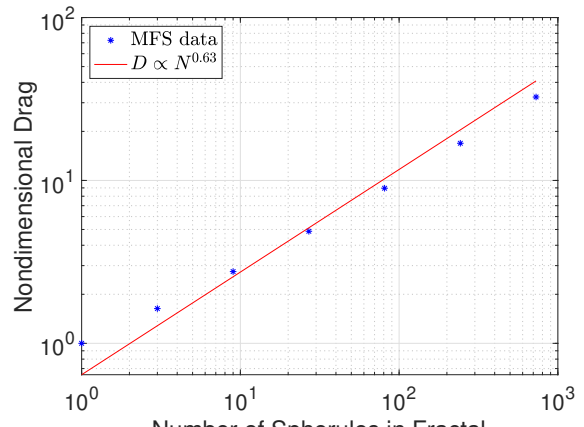
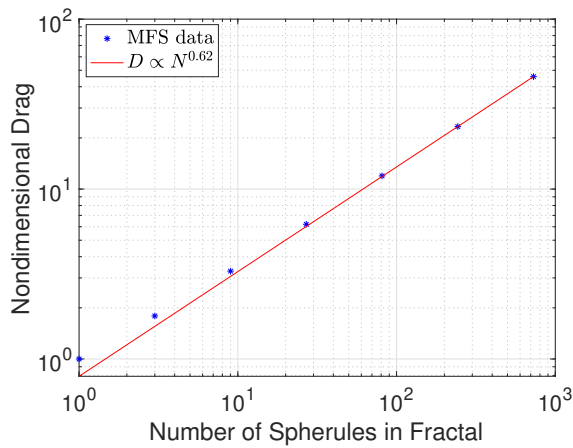
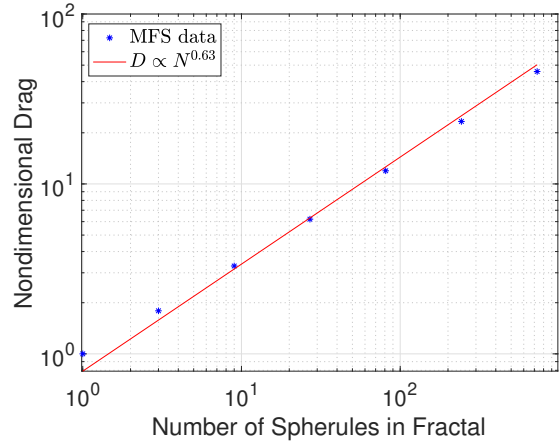
(a) Large N Fit: Velocity in the x direction.(b) $\frac{1}{D_f}$ Fit: Velocity in the x direction.(c) Large N Fit: Velocity in the z direction.(d) $\frac{1}{D_f}$ Fit: Velocity in the z direction.

Figure B.3: Drag versus number of spherules in the Sierpinski triangle fractal - 2.

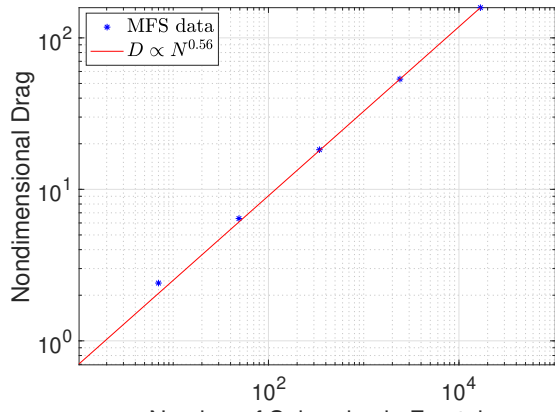
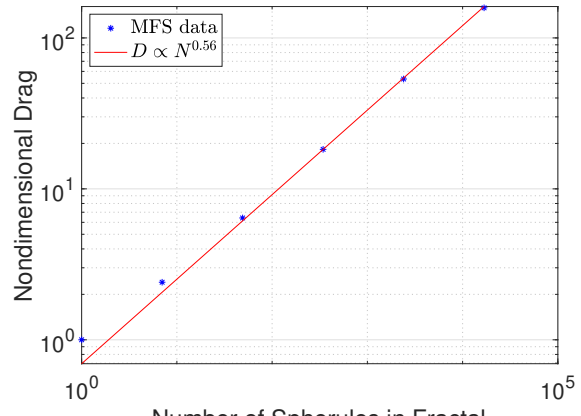
(a) Large N Fit(b) $\frac{1}{D_f}$ Fit

Figure B.4: Drag versus number of spherules in the 3D Vicsek fractal.

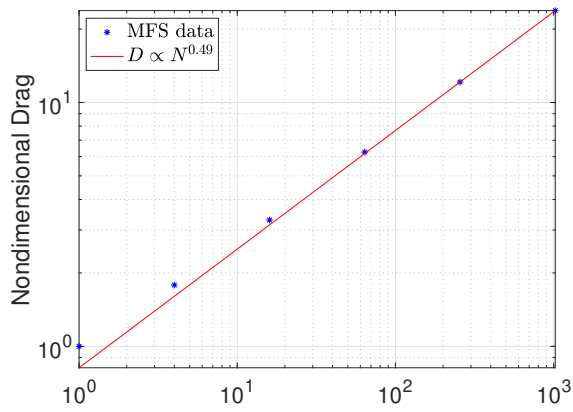
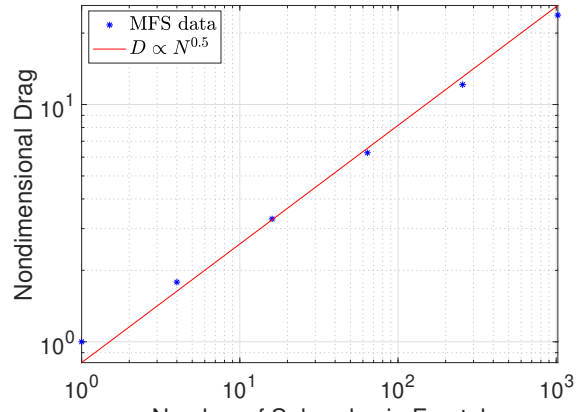
(a) Large N Fit(b) $\frac{1}{D_f}$ Fit

Figure B.5: Drag versus number of spherules in the 3D Sierpinski tetrahedron fractal.

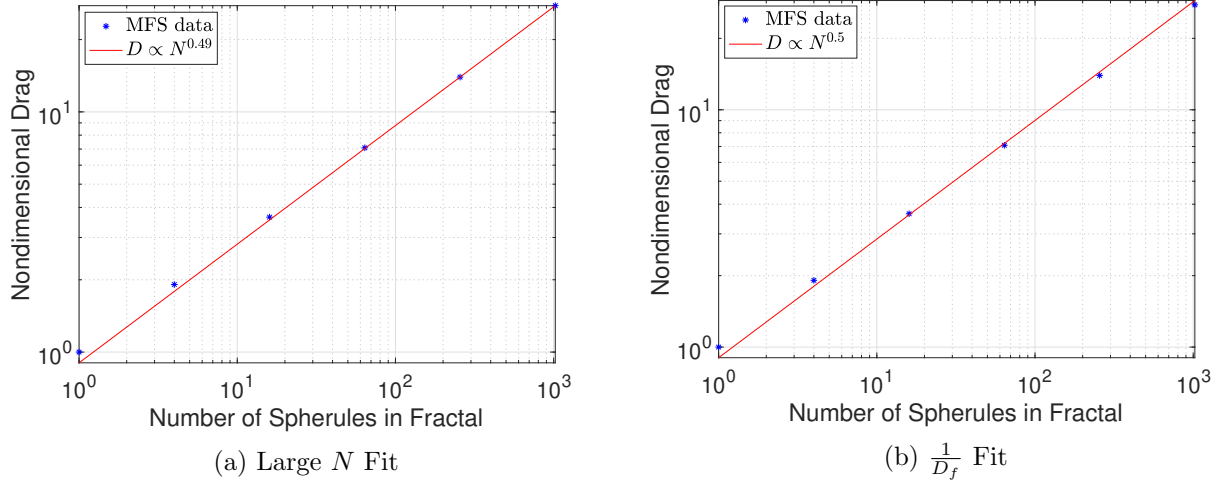


Figure B.6: Drag versus number of spherules in the 3D Sierpinski tetrahedron fractal - 2.

B.2 Drag Ratios

As observed for the chain in square, the drag ratio $\frac{D_{xy}}{D_z}$ for 2D aggregates also approaches a constant as $N \rightarrow \infty$. These plotsd are illustrated in Fig.

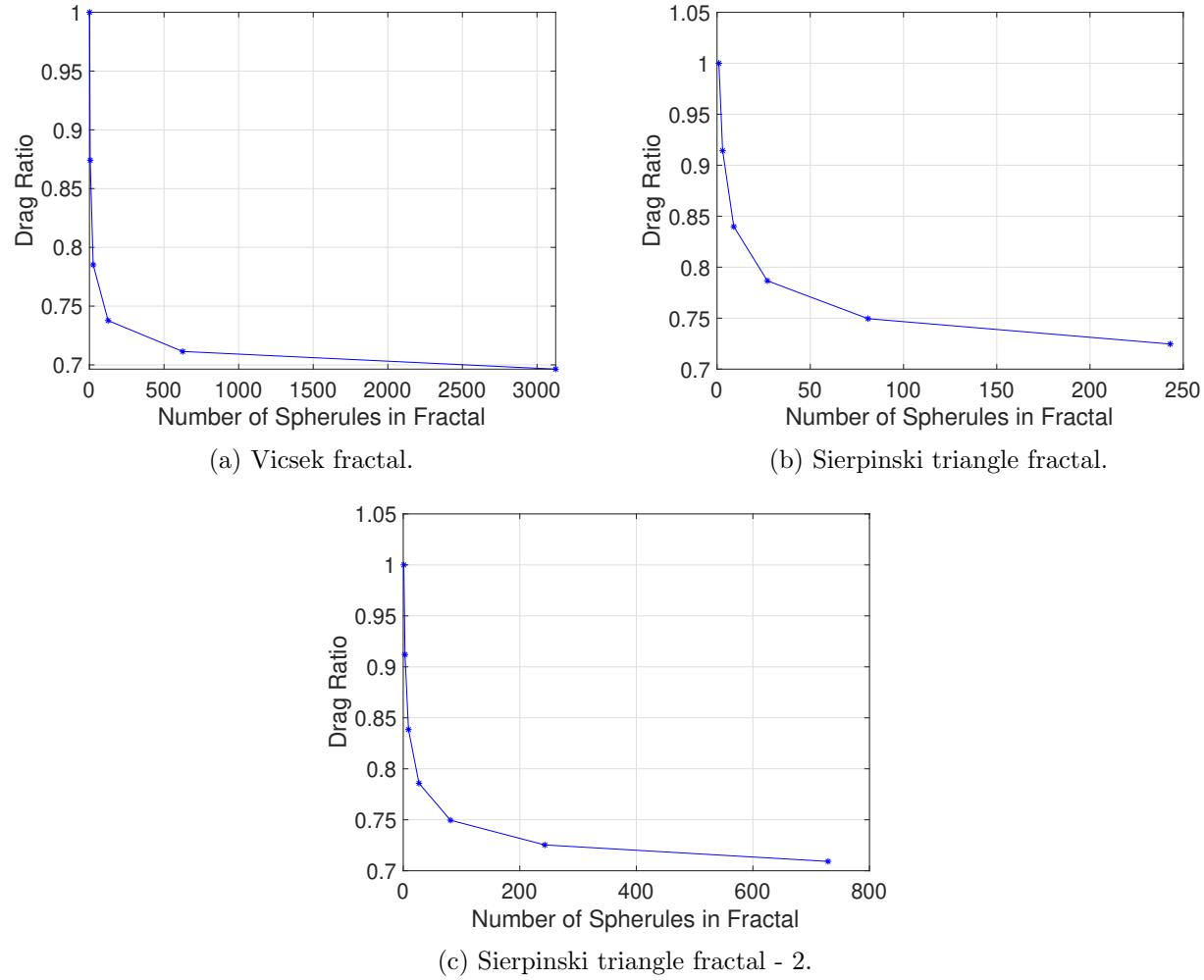


Figure B.7: Drag ratio versus number of spherules in 2D fractal aggregates.

Appendix C

Streamlines

Streamlines around a chain of spheres and the Vicsek fractal were plotted in Fig. C.1 and Fig. C.2.

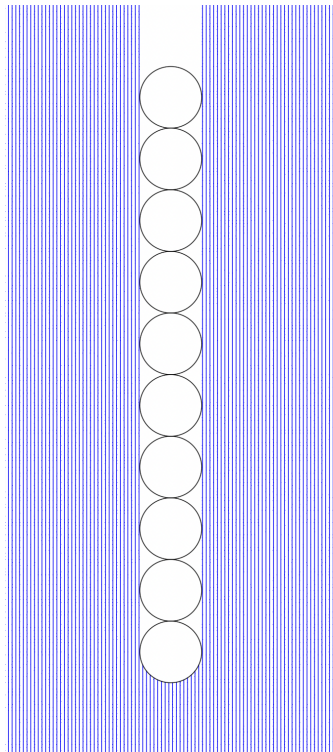


Figure C.1: Streamlines around a chain of spheres.

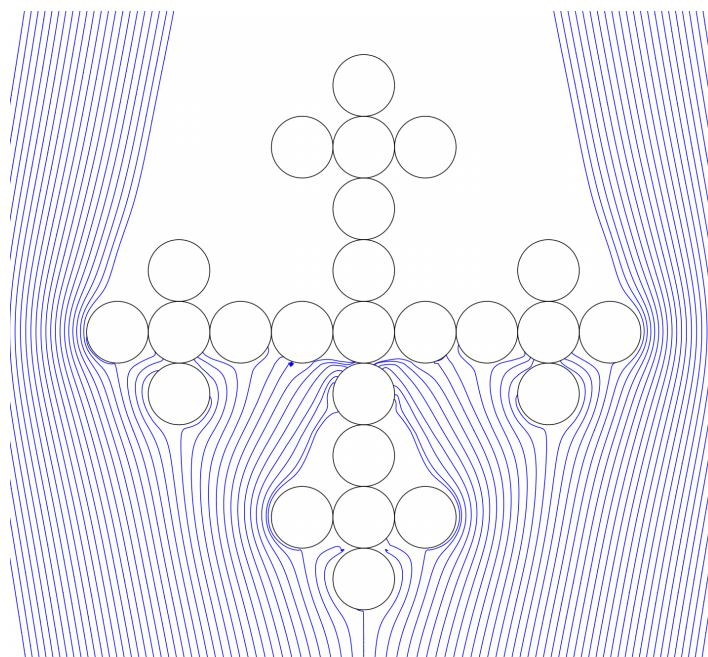


Figure C.2: Streamlines around the Vicsek fractal.